

Enhanced diapycnal mixing with polarity-reversing internal solitary waves revealed by seismic reflection data

Yi Gong¹, Haibin Song^{1*}, Zhongxiang Zhao², Yongxian Guan³, Kun Zhang¹, Yunyan Kuang¹,
Wenhao Fan¹

¹ State Key laboratory of Marine Geology, School of Ocean and Earth Science, Tongji University, Shanghai 200092, China

² Applied Physics Laboratory, University of Washington, Seattle, WA, USA

³ MNR Key Laboratory of Marine Mineral Resources, Guangzhou Marine Geological Survey, China Geological Survey, Guangzhou 510760, China

*Corresponding author. hbsong@tongji.edu.cn

Abstract

Shoaling internal solitary waves near the Dongsha Atoll in the South China Sea dissipate their energy and enhance diapycnal mixing, which have an important impact on the oceanic environment and primary productivity. The enhanced diapycnal mixing is patchy and instantaneous. Evaluating its spatiotemporal distribution requires comprehensive observation data. Fortunately, seismic oceanography meets the requirements, thanks to its high spatial resolution and large spatial coverage. In this paper, we studied three internal solitary waves in reversing polarity near the Dongsha Atoll, and calculated their spatial distribution of diapycnal diffusivity. Our results show that the average diffusivities along three survey lines are two orders of magnitude larger than the open-ocean value. The average diffusivity in internal solitary waves with reversing polarity is three times that of the non-polarity-reversal region. The diapycnal diffusivity is higher at the front of one internal solitary wave, and gradually decreases from shallow to deep water in the vertical direction. Our results also indicate that (1) the enhanced diapycnal diffusivity is related to reflection seismic events; (2) convective instability and shear instability may both contribute to the enhanced diapycnal mixing in the polarity-reversing process; and (3) the difference between our results and Richardson-number-dependent turbulence parameterizations is about 2-3 orders of magnitude, but its vertical distribution is almost the same.

[Key words] Internal solitary waves, Polarity reversal, Diapycnal mixing, Northeastern South China Sea, Seismic oceanography.

1. Introduction

Energy dissipation of internal waves enhances diapycnal mixing. Turbulence in the form of internal wave breaking is the primary mechanism for modifying thermodynamic properties in the ocean (St. Laurent et al., 2011). Small-scale changes of topography also significantly enhance local mixing (Nash and Moum, 2001; Klymak et al., 2008; Palmer et al., 2013; Staalstrøm et al., 2015; Wijesekera et al., 2020; Voet et al., 2020). Internal tides and internal waves are ubiquitous on the global continental shelves and slopes (Holloway et al., 2001; Sharples et al., 2001; Xu et al., 2010, 2016; Zhang et al., 2015; Alford et al., 2015). They play an important role in the global oceanic energy

41 balance and provide energy for ocean mixing (Mackinnon and Gregg, 2003). Due to shoaling
42 internal waves and seafloor roughness, turbulent mixing on the continental shelves and slopes is
43 more variable than in the open ocean (Carter et al., 2005). Diapycnal diffusivity observed on
44 continental shelves and slopes can span four orders of magnitude (Gregg and Özsoy, 1999; Nash
45 and Moum, 2001). Internal solitary waves are a kind of nonlinear internal wave, which usually
46 carries a large amount of energy. Numerical simulations indicate that up to 73% of the internal wave
47 energy can be carried by internal solitary waves (Bogucki et al., 1997). Therefore, internal solitary
48 waves propagating to the continental shelf and slope can greatly change the local mixing. A number
49 of researches have been carried out on mixing caused by internal solitary waves on the continental
50 shelf and slope. Observations have shown that turbulence induced by shear instability at the rear of
51 internal solitary waves sharply increases mixing (Sandstrom et al., 1989; Sandstrom and Oakey,
52 1995; Moum et al., 2003; Richards et al., 2013). Mackinnon and Gregg (2003) estimated that 50%
53 of the dissipation in the thermocline occurred with internal solitary waves. In particular, elevation
54 internal solitary waves propagating near the seafloor enhances mixing, resuspending and
55 transporting materials, which has an important impact on the local ecological environment (Klymak
56 and Moum, 2003; Moum et al., 2007).

57

58 Internal solitary waves are ubiquitous in the northeastern South China Sea (Zhao et al., 2003;
59 Klymak et al., 2006; Xu et al., 2010; Cai et al., 2012; Alford et al., 2015). They are mainly generated
60 either by nonlinear steepening of internal tides from the Luzon Strait or on local continental slope
61 (Alford et al., 2015; Xu et al., 2016; Min et al., 2019). Some internal solitary waves propagate
62 toward Dongsha Atoll, where their energy is dissipated in shoaling. The continental shelf and slope
63 of the northeastern South China Sea is close to the source, so that the amplitude and energy of
64 internal solitary waves in this area are large. The energy dissipation of internal solitary waves occurs
65 most near Dongsha Atoll and its southeastern shelf (Lien et al., 2005; Chang et al., 2006; St. Laurent,
66 2008). Observations show that high turbulence mainly occurs in the continental shelf region, and
67 the average diffusivity can reach $O(10^{-3}) \text{ m}^2 \text{ s}^{-1}$, while the diffusivity in the continental slope region
68 is one order of magnitude lower (Yang et al., 2014). When nonlinear internal waves travel cross the
69 continental slope, their waveform changes into different types (Terletska et al., 2020). In this process,
70 mixing is enhanced, and about 30% of the energy dissipation occurs near the seafloor (St. Laurent,
71 2008). The energy flux of internal solitary waves around the Dongsha Plateau is large. Lien et al.
72 (2005) estimated that, if all nonlinear internal waves break within water depth of 10 m and in an
73 area of $200 \times 200 \text{ km}^2$ centered on Dongsha Plateau, the magnitude of diffusivity can exceed $O(10^{-3})$
74 $\text{m}^2 \text{ s}^{-1}$. In addition, internal solitary waves shoaling near the Dongsha Atoll also dissipate a lot of
75 energy and improve the local mixing efficiency (Orr and Mignerey, 2003; St. Laurent et al., 2011).
76 The water in the northeastern South China Sea can exchange heat with the water in the Pacific Ocean
77 through the Kuroshio (Jan et al., 2012; Park et al., 2013; Xu et al., 2021), and heat can be transferred
78 to atmosphere through the sea-air interface on the continental shelf. Therefore, internal solitary
79 waves are an important link for energy transfer in the South China Sea and play an important role
80 in our understanding of energy transfer between the ocean and climate environment.

81

82 Turbulence in the ocean is patchy and instantaneous. Therefore, it requires extensive observations
83 to accurately evaluate turbulent mixing (Whalen et al., 2012; Waterhouse et al., 2014; Kunze, 2017).
84 Seismic oceanography (Holbrook et al., 2003) has the advantages of wide observation range and

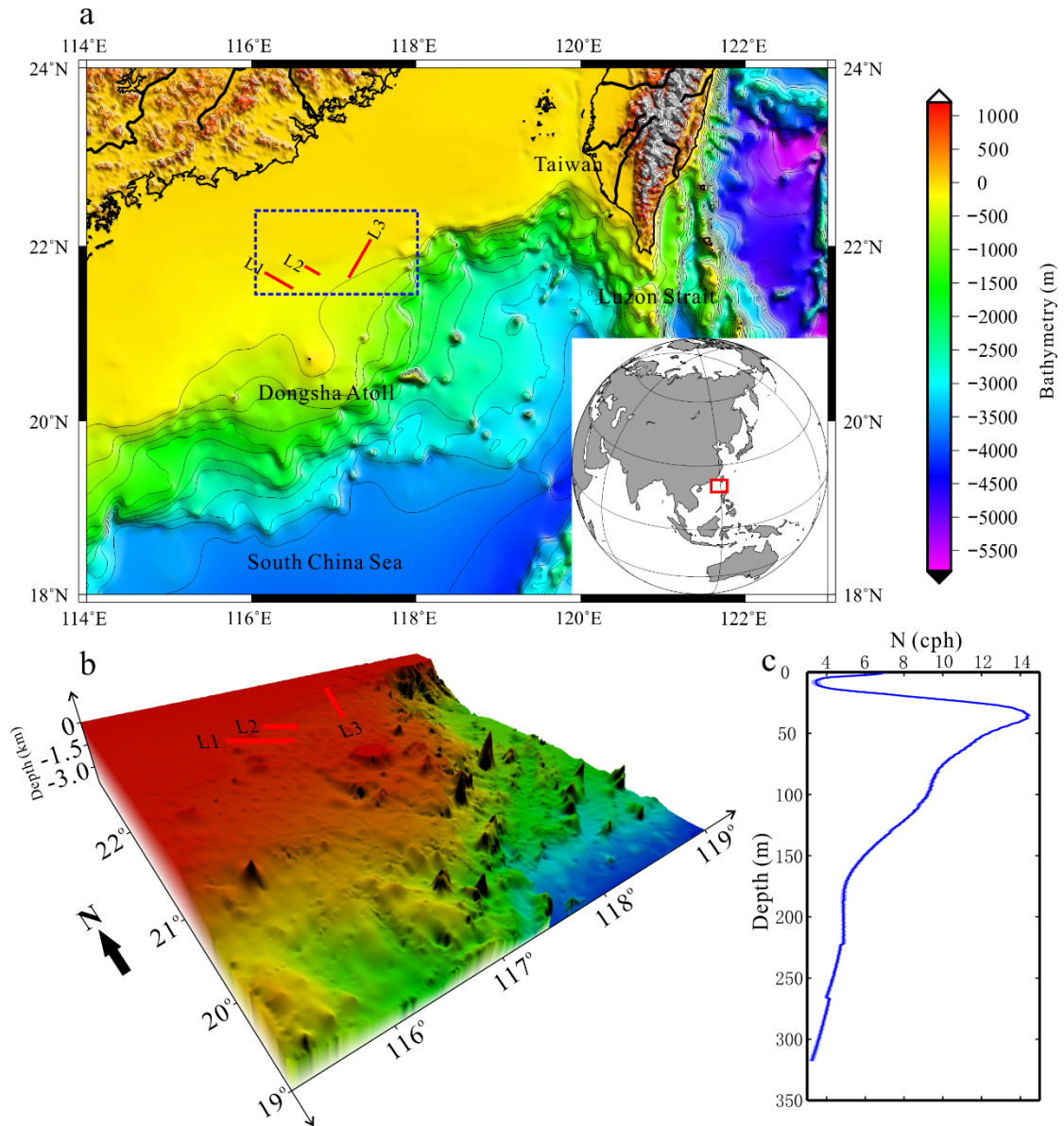
85 high spatial resolution (Ruddick et al., 2009), which is suitable for observing the spatial distribution
86 of turbulent mixing. Sheen et al. (2009) used reflection seismic data to give a diffusivity section of
87 oceanic front in the South Atlantic. Holbrook et al. (2013) comprehensively introduced the
88 theoretical basis for evaluating turbulent mixing from reflection seismic data. Subsequently, a large
89 number of scholars have used the reflection seismic method to study the spatial distribution of
90 turbulent mixing in different ocean regions or turbulent mixing induced by different ocean
91 phenomena (Fortin et al., 2016; Sallares et al., 2016; Dickinson et al., 2017; Mojica et al., 2018).

92
93 In this article, we used two-dimensional seismic data to observe the propagation of internal solitary
94 waves near the Dongsha Atoll, and calculated the spatial distribution of local diapycnal diffusivity
95 to evaluate the impact of internal solitary waves shoaling on turbulent mixing. Section 2 introduces
96 seismic data processing and the method of calculating turbulence mixing parameters. Section 3
97 describes the polarity reversal of internal solitary waves, horizontal slope spectrum and distribution
98 of turbulence diffusivity. In section 4 we analyze the relationship between diapycnal diffusivity and
99 reflection seismic events, and discuss the mechanism of turbulent mixing induced by internal
100 solitary waves. Besides, we compare the mixing scheme with our results. Section 5 gives a summary.

101 102 **2. Data and methods**

103 **2.1. Seismic data acquisition and processing**

104
105 The water is shallow on the continental shelf and slope near the Dongsha Atoll, so internal solitary
106 waves reach the transition point and their polarity changes from depression to elevation. In the
107 summer of 2009, the Guangzhou Marine Geological Survey (GMGS) set up a two-dimensional
108 seismic observation network in the Dongsha area. We found three internal solitary waves during the
109 polarity reversal process on the L1, L2, and L3 survey lines of the seismic data. The survey lines
110 are shown in Figure 1a, b. The streamer used in the acquisition process has a total length of 6 km
111 and 480 channels, the trace interval is 12.5 m, and the sampling interval is 2 ms. The airgun source
112 capacity is 5080 in³ (1 in=2.54 cm), and the main frequency of the source is 35 Hz. The shot interval
113 is 25 m, and the minimum offset is 250 m. The time interval of shots is about 10 s. Survey lines L1
114 and L2 are the in-lines, which were from the southeast to the northwest. Survey line L3 is a cross-
115 line, which was from southwest to northeast. We calculated the mean buoyancy frequency (Figure
116 1c) of the region around seismic survey lines (latitude range 21.5°-22.5°, longitude range 116°-118°,
117 blue box in Figure 1a) by reanalysis temperature and salinity data with a water depth of 100-350 m.
118 This depth range matches the observation depth of the seismic data. Besides, since the buoyancy
119 frequency changes seasonally, we only selected the buoyancy frequency from July to August in
120 2009, which matches the seismic data observation time. The hydrographic data are provided by
121 Copernicus Marine Environment Monitoring Service (CMEMS).



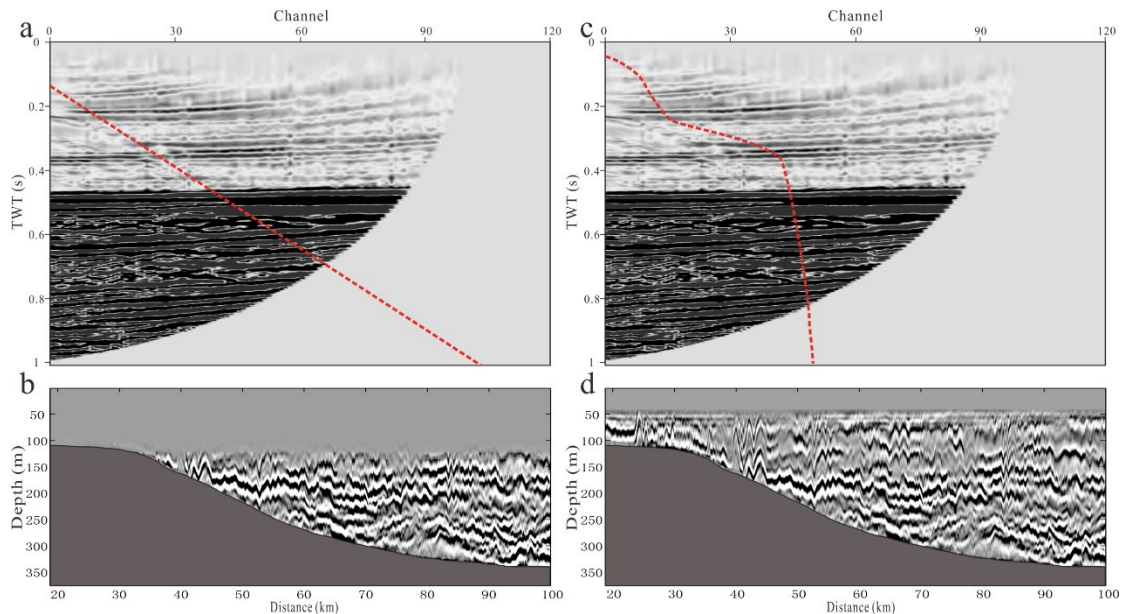
123

124 Figure 1. Bathymetry of the Dongsha area and locations of seismic survey lines. (a) 2D bathymetric map
 125 of the northeastern South China Sea, with the red lines representing the seismic survey lines. (b) 3D
 126 bathymetric map around the Dongsha Atoll. (c) The mean buoyancy frequency (cph = cycles per hour)
 127 around seismic survey lines (blue box in (a)) and its 95% confidence interval (blue shadow).

128

129 After a conventional processing of the seismic data, an image of the ocean interior's structure can
 130 be obtained. This image can be approximated as a temperature or salinity gradient map of the water
 131 column (Ruddick, et al., 2009). The conventional processing of seismic data has 5 main steps,
 132 including defining the observation system, noise and direct wave attenuation, velocity analysis,
 133 normal moveout (NMO) and horizontal stacking. Then we use a bandpass filter to filter out low-
 134 frequency noise below 8 Hz and high-frequency noise above 80 Hz. According to the linear
 135 characteristics of the direct wave, we use a median filter to extract the direct wave signal, and
 136 subtract it from the original signal to achieve the purpose of attenuating the direct wave.
 137 Subsequently, we sorted the seismic data from shot gathers into common midpoint gathers (CMPs).
 138 Sound speed is a function of depth and obtained through velocity analysis, and then the NMO is

139 applied to CMPs according to the function to flatten the reflection seismic events of the water
 140 column. When NMO is applied, the seismic wave with large offset will be stretched, and the
 141 stretched seismic waves need to be cut off. Usually, the default method is to use a linear function to
 142 remove the stretched seismic waves (Figure 2a). This may lose a lot of shallow reflection signals
 143 (Figure 2b). Bai et al. (2017) used the common offset seismic section to supplement the missing
 144 information in shallow water, but the low signal-to-noise ratio of the common offset seismic section
 145 cannot guarantee the imaging quality. In order to retain more shallow reflection signal, we used a
 146 custom function to cut off the NMO stretch (Figure 2c), thereby satisfying the imaging requirement
 147 of the shallow water column (Figure 2d). Finally, the seismic section of the water column can be
 148 obtained by stacking the processed CMPs. Due to the shallow water depth, the seismic data is
 149 seriously affected by swell noise. We filtered out the components of stacked seismic data in wave
 150 number range corresponding to swells in the frequency-wave number domain. A detailed description
 151 of the seismic data processing can be found in Ruddick et al. (2009).
 152



153
 154 Figure 2. Cutting off the stretch of NMO with a linear function (a) and the corresponding seismic section
 155 (b). Cutting off the stretch of NMO with a custom function (c) and the corresponding seismic section (d).
 156 The red dotted line shows the cut off trace, the right part of seismic data is cut off. The unit TWT of (a)
 157 and (b) is the two-way travel time of seismic wave from source to receiver.
 158

159 2.2. Diapycnal diffusivity estimates from seismic data

160
 161 Klymak and Moum (2007b) found that the horizontal wavenumber spectrum of the vertical
 162 isopycnal displacement can be interpreted as the internal wave spectrum at low wavenumbers and
 163 the turbulence spectrum at high wavenumbers. The high wavenumber components of spectrum are
 164 dominated by turbulence, and the spectral energy follows the $-5/3$ power of the wavenumber. The
 165 turbulence part of the horizontal wavenumber spectrum can be expressed by a simplified Batchelor
 166 model (Equation 2-1), so the turbulence dissipation \mathcal{E} can be estimated from the observed
 167 horizontal wavenumber spectrum. And diapycnal diffusivity can be calculated from Equation 2-2
 168 (Osborn, 1980).

169
$$\phi_{\zeta}^T = \frac{4\pi\Gamma}{N^2} C_T \varepsilon^{\frac{2}{3}} (2\pi k_x)^{-\frac{5}{3}} \quad (2-1)$$

170
$$K_{\rho} = \Gamma \varepsilon / N^2 \quad (2-2)$$

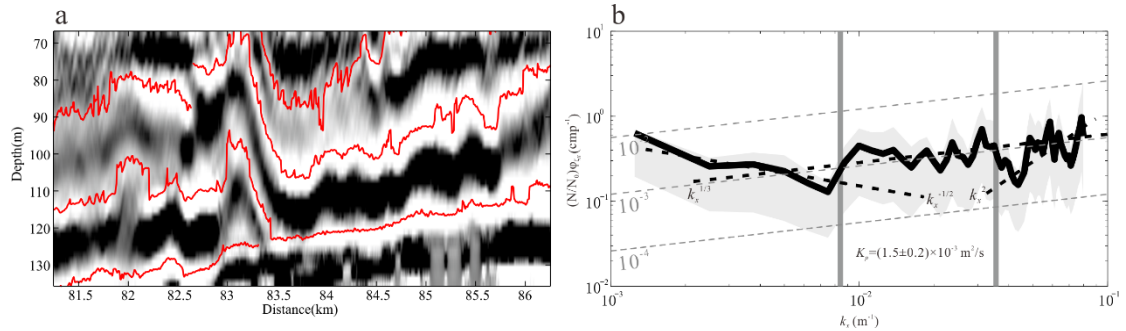
171 Where ϕ_{ζ}^T represents horizontal wavenumber spectrum, $\Gamma = 0.2$ is the mixing coefficient, N
 172 is the buoyancy frequency, $C_T = 0.4$ is the Kolmogorov constant, ε represents the turbulence
 173 dissipation, k_x is the horizontal wavenumber, and K_{ρ} represents the diapycnal diffusivity.

174
 175 Observations (Nandi et al., 2004; Nakamura et al., 2006; Sallarès et al., 2009) and simulations
 176 (Holbrook et al., 2013) show that the reflection seismic events and isopycnal are spatially consistent.
 177 Therefore, the horizontal wavenumber spectrum calculated from the vertical displacement of the
 178 reflection seismic events is equivalent to the horizontal slope spectrum that Klymak and Moum
 179 (2007b) calculated from horizontal tow measurements. The turbulence dissipation and diapycnal
 180 diffusivity can also be calculated from seismic data (Sheen et al., 2009; Holbrook et al., 2013). First,
 181 we use the seismic interpretation software to pick up reflection events in the seismic section (Figure
 182 3a). Then we calculate the vertical displacement of the reflection events. The vertical displacement
 183 is the distance of the reflection events deviate from the equilibrium position in the vertical direction.
 184 We take the mean water depth of the reflection events as the equilibrium position. Note that the
 185 choice of equilibrium position will not affect the calculation result. The spectral energy ϕ_{ζ}^T of the
 186 vertical displacement in the horizontal wavenumber domain can be obtained by Fourier transform.
 187 In practical applications, we use the slope spectrum $\phi_{\zeta_x}^T$ instead of the displacement spectrum ϕ_{ζ}^T
 188 to distinguish the turbulence subrange from the internal wave subrange. The spectral slope is as
 189 follows (Holbrook et al., 2013):

190
$$\phi_{\zeta_x}^T = (2\pi k_x)^2 \phi_{\zeta}^T \quad (2-3)$$

191 This conversion changes the wavenumber power law in the turbulence subrange from -5/3 to 1/3,
 192 so that it can be distinguished from the internal wave subrange with -1/2 power law (-5/2 in the
 193 displacement spectrum). In calculating the turbulence dissipation in the seismic section, it is
 194 necessary to grid the section and calculate the dissipation in each grid separately. The horizontal
 195 grid is set as 5 km, and the grid step 2.5 km. As the water depth in the seismic data is shallow, the
 196 reflection seismic events are less in the vertical direction. In order to ensure more than two events
 197 in each grid, we set the vertical grid to be 75 m and the grid step 37.5 m. In each grid, we calculated
 198 the spectral slope of each event and took the average as $\overline{\phi_{\zeta_x}^T}$. We fitted the averaged spectrum in
 199 the turbulence subrange to the Equation 2-1 and calculated the turbulence dissipation ε . To reduce
 200 uncertainty, we only calculated the cases with a length >1000 m in each grid. Experiments showed
 201 that this length can correctly represent the slope of energy spectra in turbulence subrange (Figure
 202 3b). After traversing all the grids, the turbulent dissipation section is obtained, and the diapycnal
 203 diffusivity section can be obtained as well according to Equation 2-2. The uncertainty of the

204 turbulence dissipation and diapycnal diffusivity was evaluated by the error between observed
 205 average slope spectrum and the fitted Batchelor model (see Appendix). We used a spline smoothing
 206 function to smooth the meshing results.
 207



208
 209 Figure 3. (a) The reflection seismic events in a grid. (b) The average horizontal slope spectrum (black
 210 line). The gray shadow represents the 95% confidence interval. The gray dashed lines represent the
 211 diffusivity contour. The black dashed lines represent the spectral slopes in internal wave subrange,
 212 turbulence subrange and noise subrange, respectively. The gray vertical lines indicate the boundaries of
 213 turbulence subrange.
 214

215 2.3. Estimating the horizontal wave-induced velocity of internal solitary waves

216
 217 We estimated the wave-induced horizontal velocity of internal solitary waves according to the
 218 method proposed by Moum et al. (2007). This method requires the observational data to satisfy two
 219 assumptions: 1) the isopycnal is parallel to the streamline; 2) the internal solitary wave satisfies the
 220 KdV equation. Moum et al. (2007) picked the isopycnal from the high-frequency acoustic section
 221 and fitted it with the KdV equation. The displacement equation of isopycnal can be obtained, and
 222 the derivation of displacement equation is the wave-induced velocity. Seismic data satisfy the first
 223 assumption. Although breaking induced polarity reversal of internal solitary waves close the
 224 streamlines, it is difficult to record reflection seismic data from those areas with closed streamline
 225 at the resolution scale of seismic data. The regional density gradient recorded by the reflection
 226 events still exists, and the streamline is parallel to the isopycnal at this time. While areas with closed
 227 streamlines are strongly mixed, and the density gradient weakens or even disappears, which cannot
 228 be recorded in seismic data. Unfortunately, the internal solitary waves we observed do not satisfy
 229 the second assumption. The KdV equation can simulate internal solitary waves with small amplitude
 230 and weak nonlinearity, but the polarity reversal of the large-amplitude internal solitary waves we
 231 observed cannot be simulated well. Here we did not use theoretical models to fit observations.
 232 Although there are studies using theory to successfully simulate the polarity reversal of internal
 233 solitary waves (Liu et al., 1998; Zhao et al., 2003), it is difficult to match theories and observations.

234 We used the picked reflection seismic events to calculate the isopycnal displacement $\eta(x, z)$
 235 (Figure 4b). $\eta(x, z)$ is the distance that reflection seismic events deviate from the equilibrium
 236 position, which is determined by the mean depth of two shoulders of one internal solitary wave
 237 (Figure 4a). We smoothed $\eta(x, z)$ with a spline function same as that was used for smoothing

238 turbulence dissipation, so that the resolution of wave-induced velocity is consistent with that of
 239 turbulence dissipation. Therefore, the stream function can be expressed as (Holloway et al., 1999):

$$240 \quad \Psi(x, z) = c\eta(x, z) \quad (2-4)$$

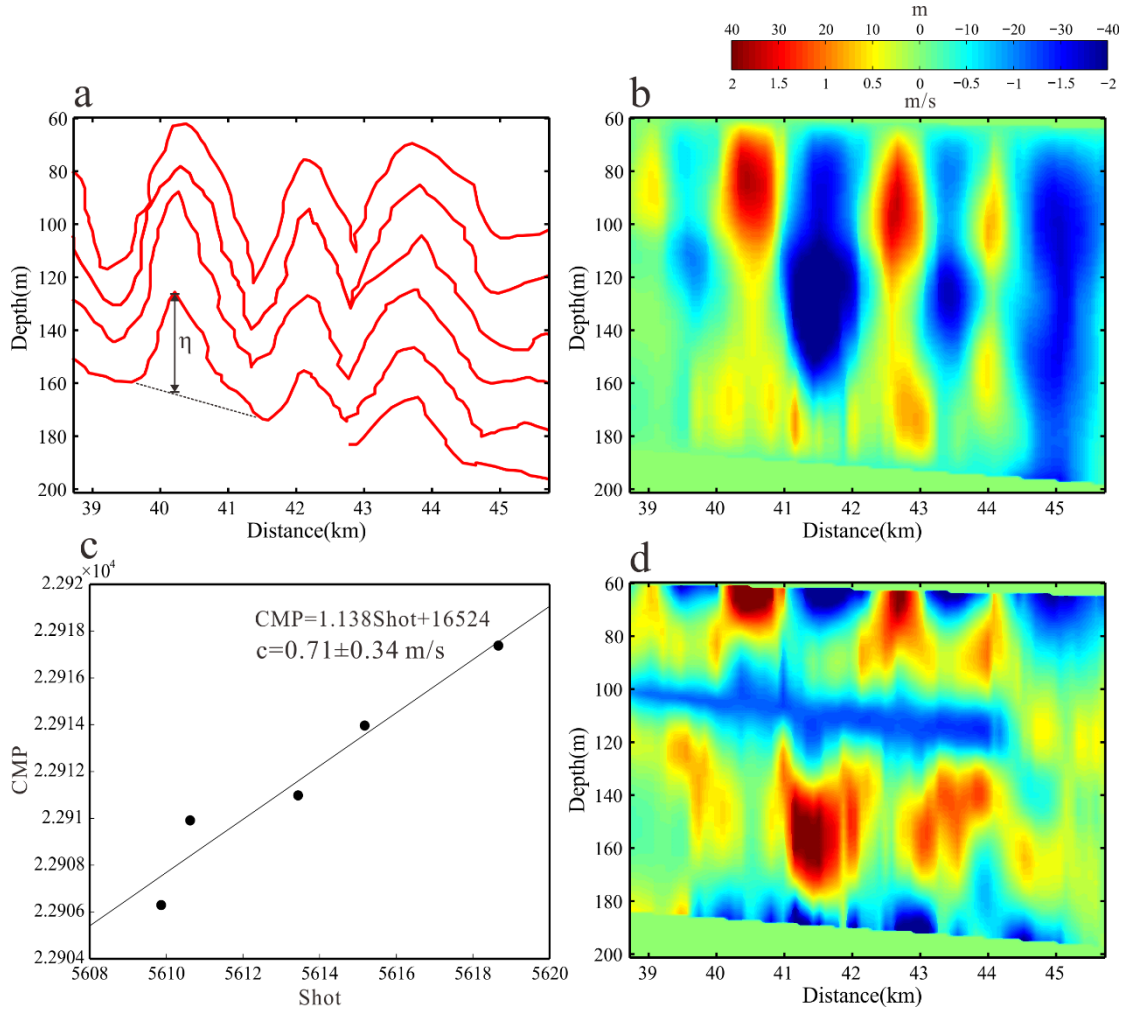
241 where c is the phase velocity of internal solitary waves. c can be estimated from pre-stack
 242 seismic data (Tang et al., 2014, 2015; Fan et al., 2021). The seismic data is redundant, because we
 243 have made multiple observations of the same events, which allows us to study the movement of the
 244 water column. Specifically, after sorting the seismic data into CMPs (section 2.1), we extracted
 245 traces with the same offset from CMPs to form common offset gathers (COGs). Multiple COGs can
 246 be obtained in the order of offset from small to large. The larger the offset, the lower the signal-to-
 247 noise ratio of the data. We selected the first five COGs to ensure the imaging quality. Pre-stack
 248 migration of COGs yields COG sections, which show images of the same water column at different
 249 times. Tracking the change of shot-receiver pairs at a certain reflection point yields the phase
 250 velocity (Fan et al., 2021). Figure 4c shows the change of the shot-receiver pairs of internal solitary
 251 wave trough in the L1 survey line. The straight line represents the fitting line of the shot-receiver
 252 pairs. The average phase velocity of the internal solitary wave during the imaging time is

$$253 \quad c = \frac{d_{cmp}}{dt_s} k, \text{ where } d_{cmp} \text{ is the half of the trace interval, } dt_s \text{ the time interval of shot, and } k$$

254 the slope of the fitted line. After calculating the flow function according to Equations 2-4, the wave-
 255 induced horizontal velocity can be expressed as

$$256 \quad u(x, z) = \frac{\partial \Psi}{\partial z} \quad (2-5)$$

257



258

259 Figure 4. (a) Schematic of calculating internal solitary wave isopycnal displacement using reflection
 260 seismic events. (b) The isopycnal displacement section of internal solitary wave. (c) Calculating the mean
 261 phase velocity of internal solitary wave by pre-stack seismic data. (d) The wave-induced horizontal
 262 velocity.

263

264 The wave-induced velocity here is on the seismic-resolution scale, which should be taken as its low-
 265 frequency component only. The results are insufficient to characterize the high-frequency
 266 components. But this rough wave-induced velocity is useful, because our purpose of calculating
 267 wave-induced velocity is for the vertical mixing scheme. The wave-induced velocity makes the
 268 resolution scale of the mixing scheme equal to that of mixing parameters estimated from the seismic
 269 data, and the two are comparable. In addition, the error of the wave-induced velocity is mainly
 270 determined by the error of the phase velocity of the internal solitary wave. For internal solitary
 271 waves with polarity reversal, the error of the phase velocity is large, because the phase velocity
 272 gradually decreases when the internal solitary wave is shoaling (Bourgault et al., 2007; Shroyer et
 273 al., 2008). It can be seen from Figure 4c that the shot-receiver pairs do not completely fall on the
 274 fitted line.

275

276 2.4. Mixing scheme for internal solitary wave shoaling

277

278 Shoaling and breaking of internal solitary waves on the continental shelf and slope enhance mixing.
 279 Vlasenko and Hutter (2002) studied the breaking of internal solitary waves over slope-shelf
 280 topography by numerical simulation. In their model, the mixing scheme (PP scheme) proposed by
 281 Pacanowski and Philander (1981) was improved, and a vertical mixing scheme for resolving
 282 breaking internal solitary waves was given. In this scheme, the vertical turbulence kinematic
 283 viscosity and diffusivity are determined by the Richardson-number-dependent turbulence
 284 parameterizations. The expression is as follows:

$$285 \quad Ri = \frac{N^2}{u_z^2} \quad (2-6)$$

$$286 \quad \nu = \frac{V_0}{(1 + \alpha Ri)^n} + \nu_b \quad (2-7)$$

$$287 \quad \kappa = \frac{V_0}{(1 + \alpha Ri)^n} + \kappa_b \quad (2-8)$$

288 Where u_z is the vertical gradient of horizontal wave-induced velocity, ν is vertical turbulence
 289 kinematic viscosity, κ is vertical turbulence kinematic diffusivity. Vlasenko and Hutter (2002)
 290 selected the best model parameters after a series of experiments. They are $\nu_0 = 10^{-3} m^2 s^{-1}$,
 291 $\nu_b = 10^{-5} m^2 s^{-1}$, $\kappa_b = 10^{-6} m^2 s^{-1}$, $\alpha = 5$ and $n = 1$. Based on this model, they simulated the
 292 process of internal solitary wave shoaling and breaking on slope-shelf topography and studied the
 293 breaking criterion.

294

295 **3. Results**

296 **3.1. Polarity reversal of internal solitary wave in seismic section**

297

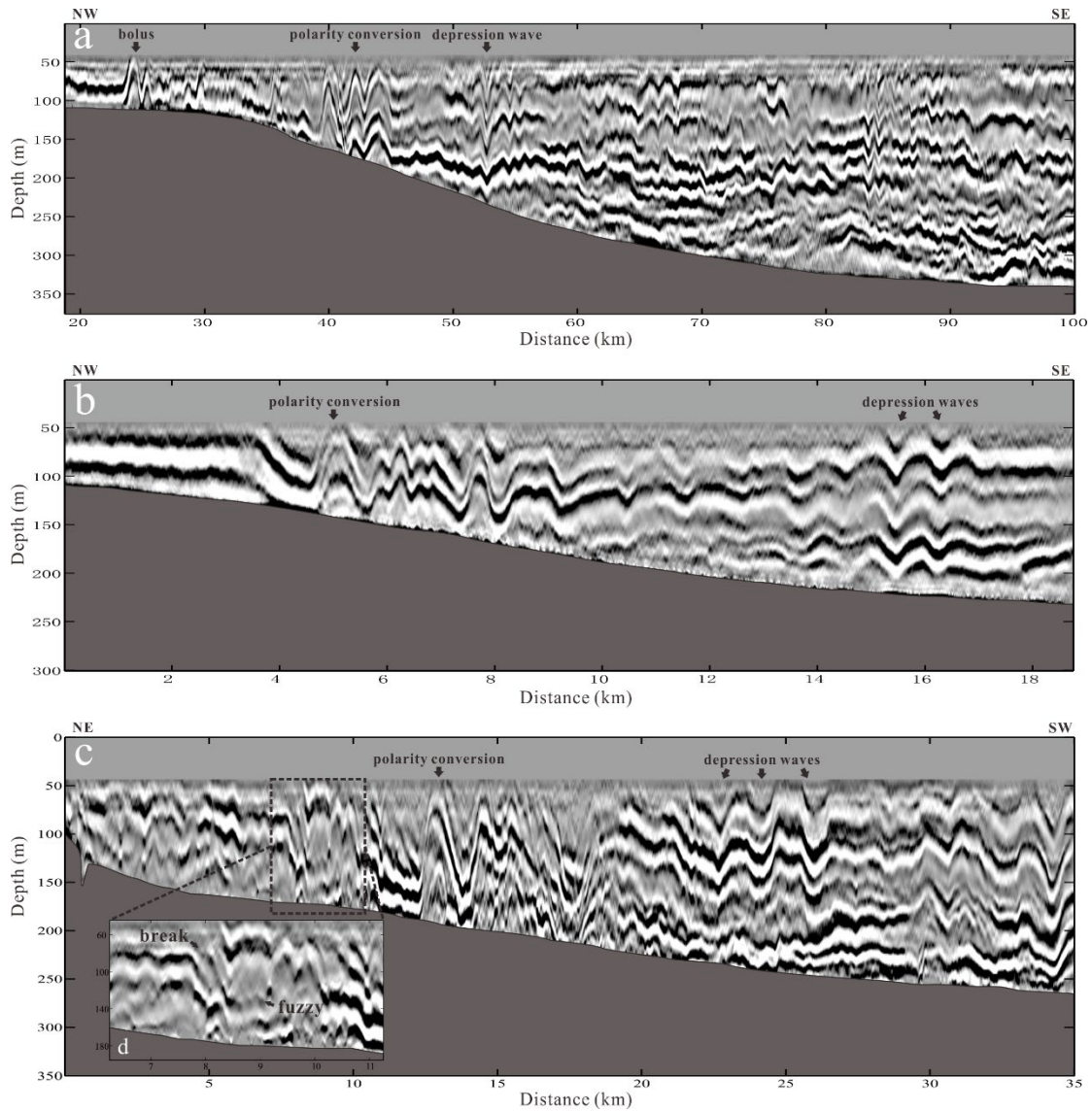
298 When one internal solitary wave propagates cross the transition point, it converts from a depression
 299 wave to an elevation wave. In the two-layer ocean model, the transition point is defined as the
 300 position where the pycnocline is close to the mid-depth (Grimshaw et al., 2010). The three seismic
 301 sections in Figure 5 capture the images of internal solitary waves passing the transition point. Figure
 302 5a is the seismic section of survey line L1. It shows that the water depth becomes shallower from
 303 southeast to northwest, and the bottom slope is steeper between 30-60 km. In the deep-water region
 304 of 60-100 km, internal waves are developed, and the reflection seismic events fluctuate obviously.
 305 Near the seafloor around 80 km, the reflection seismic events are uplifted and discontinuous,
 306 forming a fuzzy reflection area. A mode-1 depression internal solitary wave can be identified at 53
 307 km, indicating that the transition point has not been reached yet. The internal solitary wave has
 308 reversed polarity at 40 km, and a packet of three elevation waves is formed. The reflection seismic
 309 events are continuous here, implying no wave breaking. Five elevation waves can be identified
 310 around 24-37 km, among which four elevation waves at 24 km may be formed continuously, while
 311 the elevation wave at 37 km is formed later.

312

313 Figure 5b gives another internal solitary wave polarity reversal process captured by the survey line
314 L2. There are two obvious depression waves at 16 km. There are multiple waves with smaller
315 amplitude around 10-15 km. The polarity of internal solitary wave is reversing within 4-8 km. The
316 length of the head wave becomes wider and the slope becomes gentler. The leading wave is followed
317 by a packet of multiple elevation waves. The reflection seismic events are continuous in the whole
318 section.

319

320 L3 is a cross line whose observation direction is perpendicular to survey line L1 and L2 (Figure 5c).
321 There are multiple depression waves with large amplitudes of 20-35 km, and the reflection seismic
322 events are continuous. The wave polarity is reversing within 10-20 km, and the reflection seismic
323 events are discontinuous in this region. At 10 km, there is a large-amplitude elevation internal
324 solitary wave, and the wave front is almost parallel to seafloor. There is a large-amplitude depression
325 wave at 17 km, and the wave trough has interacted with topography. Most of the reflection seismic
326 events before 10 km are discontinuous and fuzzy, especially in the range of 6-10 km (Figure 5d). It
327 indicates that the reflective structures in this region may be destroyed by internal solitary wave
328 breaking. It should be noted that the breaking mentioned in this article refers to local breaking caused
329 by instability, not the four types of classic breaking (Aghsaee et al., 2010).
330



331

332 Figure 5. The seismic sections of survey line L1 (a), L2 (b) and L3 (c). The gray regions in the sections
 333 represent seafloor. Internal solitary waves can be seen in all three cases. The subfigure (d) is the enlarged
 334 regional image of 6-10 km.

335

336 3.2. The horizontal slope spectrum

337

338 We picked the reflection seismic events in the three sections (Figure 7) and calculated the horizontal
 339 slope spectrum using the method described in section 2.2. Figure 6 shows the average horizontal
 340 slope spectrum of the three sections. We calculated the horizontal slope spectrum of all tracked
 341 events and averaged in logarithmic space to determine the wavenumber of turbulence subrange. The
 342 turbulence subrange of the survey line L1 section is $0.005-0.069 \text{ m}^{-1}$, as shown by the gray vertical
 343 line in Figure 6a. The corresponding wavelength is 15-200 m. The average diapycnal diffusivity is
 344 $(7.0 \pm 1.2) \times 10^{-4} \text{ m}^2/\text{s}$, which is one order of magnitude larger than the open-ocean value ($10^{-5} \text{ m}^2/\text{s}$).
 345 The spectral energy in internal wave subrange is larger than that in turbulence subrange, indicating
 346 that the energy is dominated by internal waves. This is confirmed by internal waves in the seismic
 347 sections. The difference from Holbrook et al. (2013) is that the calculated horizontal slope spectrum

348 does not include harmonic noise. This may be because harmonic noise has been removed when we
349 filtered out the swell noise. In addition, we have not smoothed the events, so some high-
350 wavenumber ranges are reserved. If the events are smoothed, the spectral energy will decrease
351 rapidly in the high-wavenumber range (Holbrook et al., 2013; Tang et al., 2019).

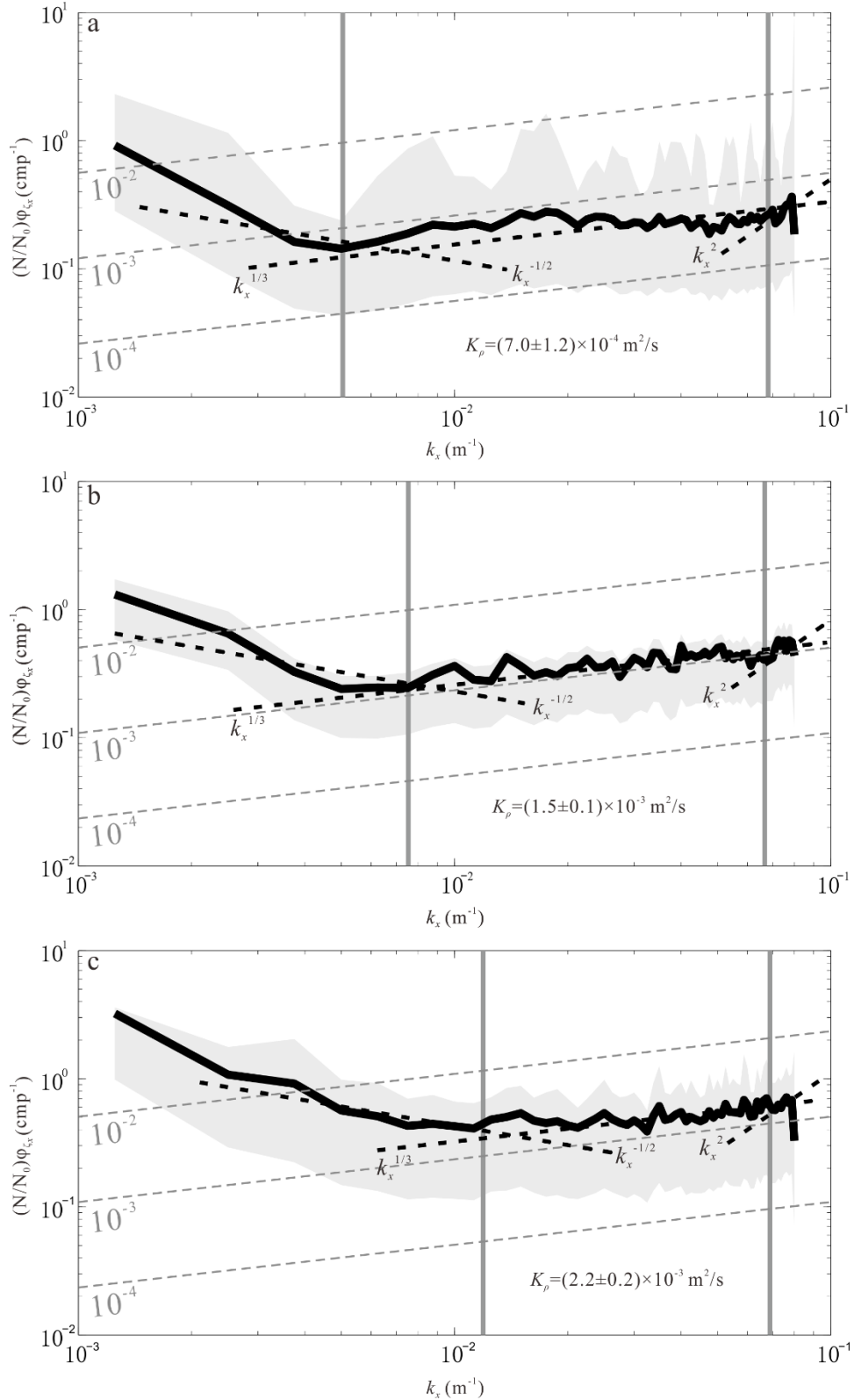
352

353 The horizontal slope spectrum of the L2 section is shown in Figure 6b. The turbulence subrange is
354 $0.008-0.068 \text{ m}^{-1}$, and the corresponding wavelength is 15-133 m. Compared with the survey line L1,
355 the turbulence shifts to a smaller scale. The spectral energy in internal wave subrange has the same
356 order of magnitude as the spectral energy in turbulence subrange, which indicates that the energy is
357 transferring to small-scale turbulence. This process is closely related to the polarity reversal of
358 internal solitary waves. The average diapycnal diffusivity is $(1.5\pm 0.1)\times 10^{-3} \text{ m}^2/\text{s}$, which is two
359 orders of magnitude larger than the background value.

360

361 Figure 6c is the horizontal slope spectrum of the L3 section. It can be seen from the spectrum that
362 the turbulence subrange is small, ranging from $0.011-0.07 \text{ m}^{-1}$. The corresponding wavelength is
363 14-89 m. The internal wave energy is larger and occupies a larger scale range. It can be seen from
364 the seismic section of survey line L3 (Figure 5c) that the wave amplitudes are large. It indicates that
365 the internal waves carry more energy, so the spectral energy in internal wave subrange is larger
366 (Figure 6c). In addition, there are many discontinuous and weak reflections in the seismic section
367 caused by breaking internal solitary waves. Internal solitary wave breaking weakens the density
368 gradient and enhances local mixing. This phenomenon is most typical in the survey line L3, where
369 the average diffusivity $(2.2\pm 0.2)\times 10^{-3} \text{ m}^2/\text{s}$ is the largest of the three sections.

370



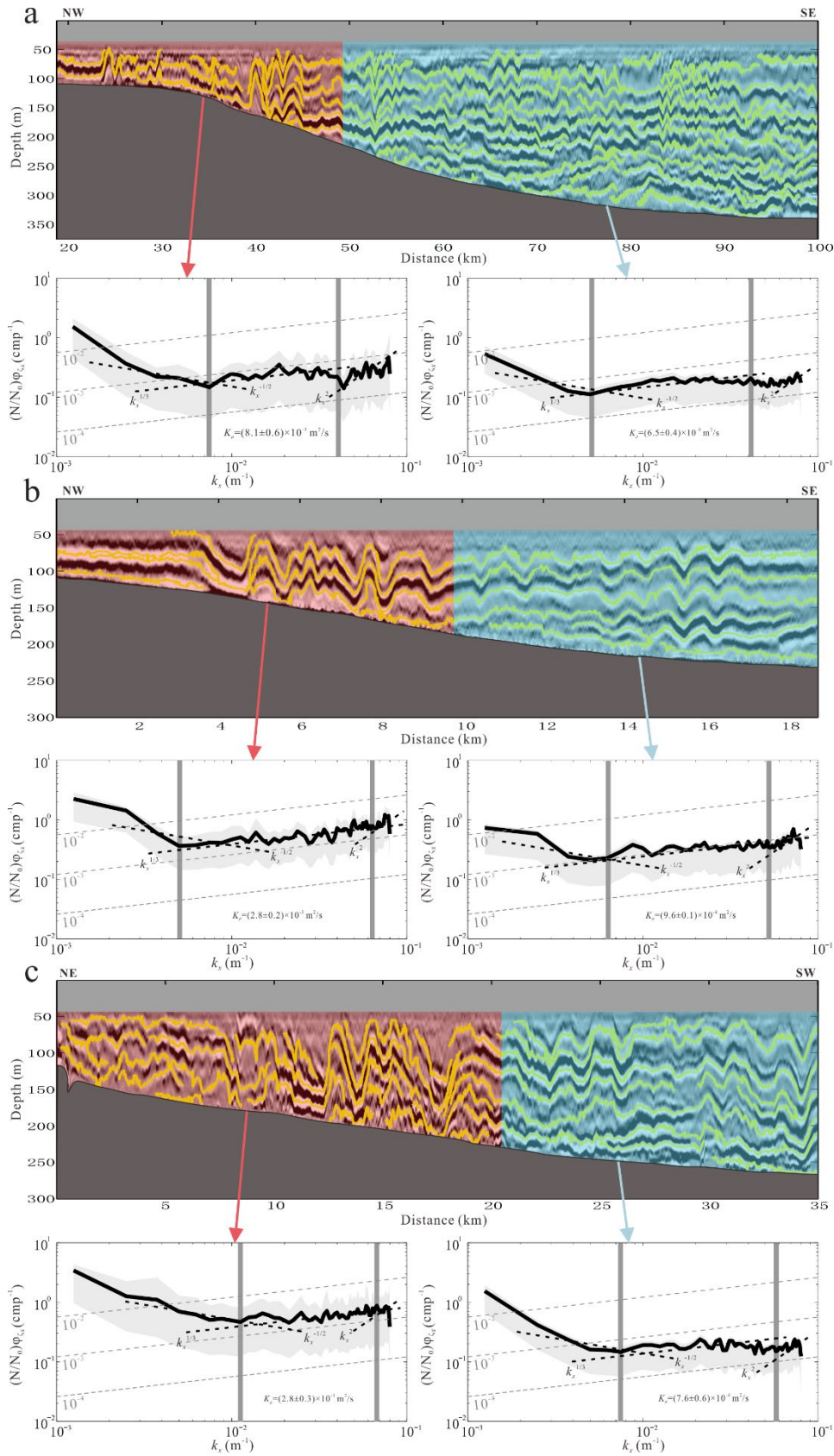
371

372 Figure 6. The average horizontal slope spectra of L1 section (a), L2 section (b) and L3 section (c). The
 373 black line is the spectrum, the gray shadow represents the 95% confidence interval, the gray dashed lines
 374 represent the diffusivity contour, the black dashed lines represent the spectral slopes in internal wave
 375 subrange, turbulence subrange and noise subrange, respectively. The gray vertical lines label the
 376 boundaries of turbulence subrange.

377

378 Figure 6 shows that the spectral energy of the L1 section is smaller than that of the other two sections.
379 This may be because the imaging range of the L1 section is different. The observations in the L2
380 and L3 sections are the polarity reversal of internal solitary waves, while the L1 section includes
381 not only the polarity reversal process, but also internal waves in deep water. The spectral energies
382 of these two processes should be different. We calculated the average horizontal slope spectrum of
383 the polarity reversal region and the non-polarity reversal region, respectively (Figure 7). The
384 spectral energy of the polarity reversal region in L1 section is higher than that of the non-polarity
385 reversal region, so does diapycnal diffusivity (Figure 7a). It implies that the wave energy will
386 accelerate to dissipate and transfer to turbulence when its polarity is reversed. Compared with the
387 non-polarity reversal region, the turbulence subrange of the polarity reversal region is smaller. The
388 lower boundary of the turbulence subrange of the polarity reversal region is slightly larger than that
389 of the non-polarity reversal region. It indicates that the turbulence in this region has a smaller scale.
390 The diapycnal diffusivity in the polarity reversal region in L2 section is about 3 times that of the
391 non-polarity reversal region (Figure 7b). The turbulence subrange of the polarity reversal region in
392 L2 section is slightly larger than that of the non-polarity reversal region. From the L2 section, it can
393 be seen that the events are continuous during the polarity reversal process, which indicates that the
394 wave breaking is weak. The internal solitary wave gradually fissions into several tails during the
395 polarity reversal, and energy is dissipated constantly. Therefore, there will be a large turbulence
396 subrange in the lateral direction (Figure 7b). This process can dissipate much more energy compared
397 with direct breaking of internal solitary waves (Masunaga et al., 2019). The diapycnal diffusivity in
398 the polarity reversal region in L3 section is larger, more than 3 times that of the non-polarity reversal
399 region. Although there are more internal (solitary) waves with larger amplitude in the non-polarity
400 reversal region, the diapycnal diffusivity is lower. The polarity reversal of internal solitary waves
401 significantly increases the diapycnal diffusivity. The turbulence subrange of the polarity reversal
402 region is small, and the lower boundary of the turbulence subrange is greater than 0.01 m^{-1} .

403



404

405 Figure 7. The horizontal slope spectra of the polarity reversal and non-polarity reversal regions calculated

406 from L1 section (a), L2 section (b) and L3 section. The yellow lines are tracked reflection seismic events.

407

408 3.3. Diapycnal diffusivity maps

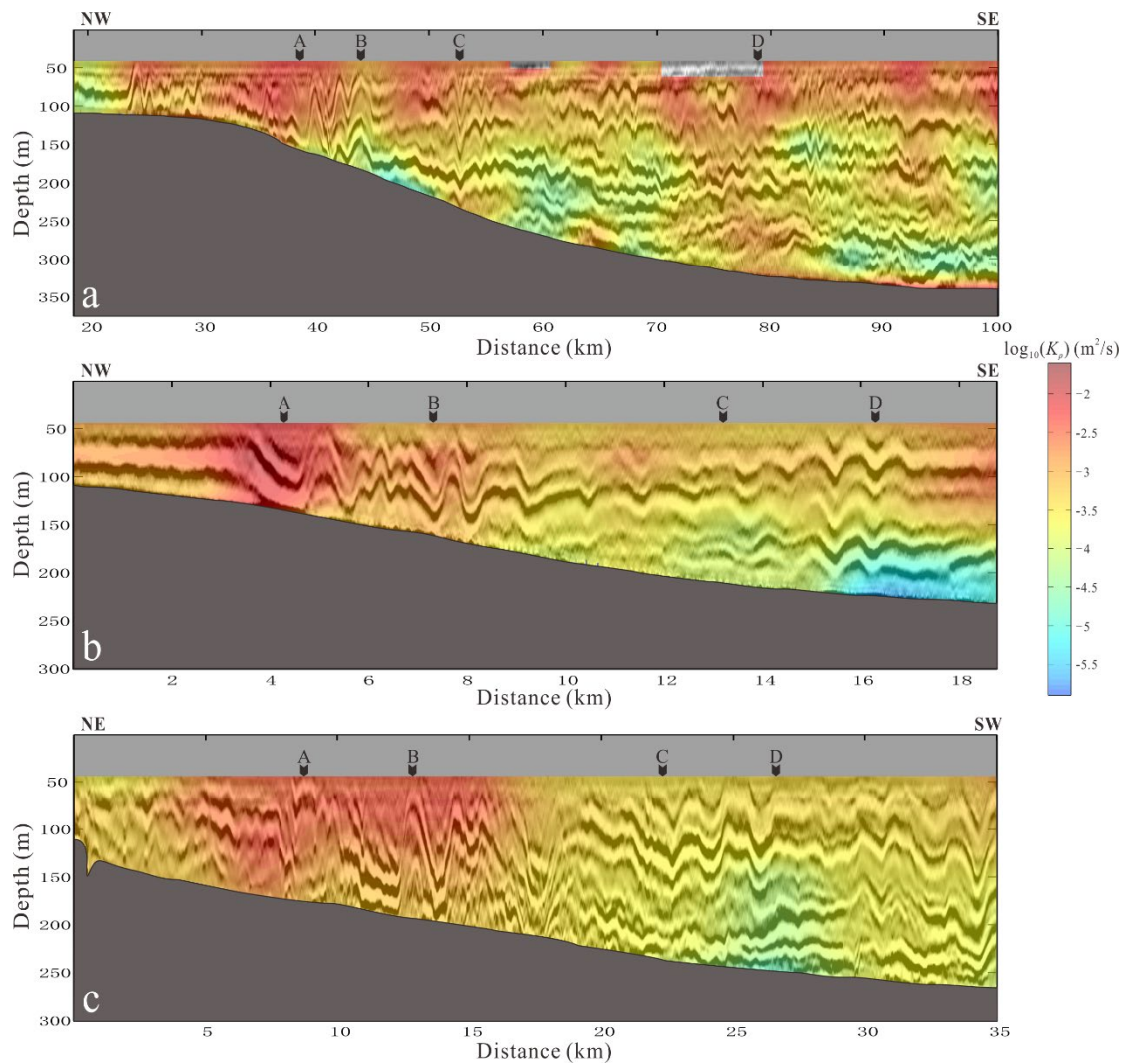
409

410 The diapycnal diffusivity maps of the three survey lines are shown in Figure 8. Figure 8a shows the
411 map of the survey line L1. The diffusivity is higher than that of the open ocean. The high value
412 presents a patchy distribution, mainly distributed in the depth between 50-150 m. The low diffusivity
413 values are mainly distributed in the depth between 150-300 m. Some high values are also distributed
414 near the seafloor. The diffusivity is larger in the polarity reversal region (24-45 km). Compared the
415 diffusivity of the four adjacent elevation internal solitary waves (24-30 km), we find that the
416 diffusivity is proportional to the amplitude of internal solitary waves. It means that the large
417 amplitude internal solitary waves contribute more to mixing. In the polarity reversal region (40-45
418 km), the diffusivity of the head wave's front is higher, that is, where the slope of the wave front
419 becomes gentle. While the diffusivity of the two elevation waves followed the head wave is small.
420 It indicates that the mixing induced by internal solitary wave polarity reversal is stronger at the
421 beginning, and more energy is dissipated at this time. In the non-polarity reversal region (50-100
422 km), the diffusivity is low. The mode-1 depression internal solitary wave at 52 km increases the
423 diffusivity. There is an abnormal reflection area near the seafloor at 80 km, and the diffusivity is
424 high. In addition, there is also an area with increased diffusivity between 100-250 m at 93 km. This
425 may be related to large-amplitude internal waves.

426

427 The diffusivity map of the survey line L2 is shown in Figure 8b. The high value is mainly distributed
428 at the front of head wave during polarity reversal process (4 km), which is consistent with the
429 characteristics on L1. The diffusivity after the head wave is low, but it is still higher than that in
430 other regions. The diffusivity in the non-polarity reversal region is almost uniform. The two internal
431 solitary waves at 15-16 km did not increase the diffusivity. There is a low diffusivity area near the
432 seafloor around 16-18 km, which is caused by not tracked reflection seismic events in this area. The
433 diffusivity map of survey line L3 (Figure 8c) is similar to that of L2. The high value is distributed
434 in the polarity reversal region and the diffusivity of head wave is still high. However, unlike the
435 diffusivity map of L2, the high diffusivity is mainly distributed in the shallow part of the head wave
436 (water depth 50-120 m), while the diffusivity of the whole head wave in L2 is high. In the non-
437 polarity reversal region, the diffusivity is small and the distribution is uniform too. The diffusivity
438 near the seafloor at 25-27 km is slightly lower than other regions.

439



440

441 Figure 8. The diapycnal diffusivity map of survey line L1 (a), L2 (b) and L3 (c). The black arrows
 442 represent the position of vertical diffusivity profile.

443

444 4. Discussions

445 4.1 The relationship between diffusivity and reflection seismic events

446

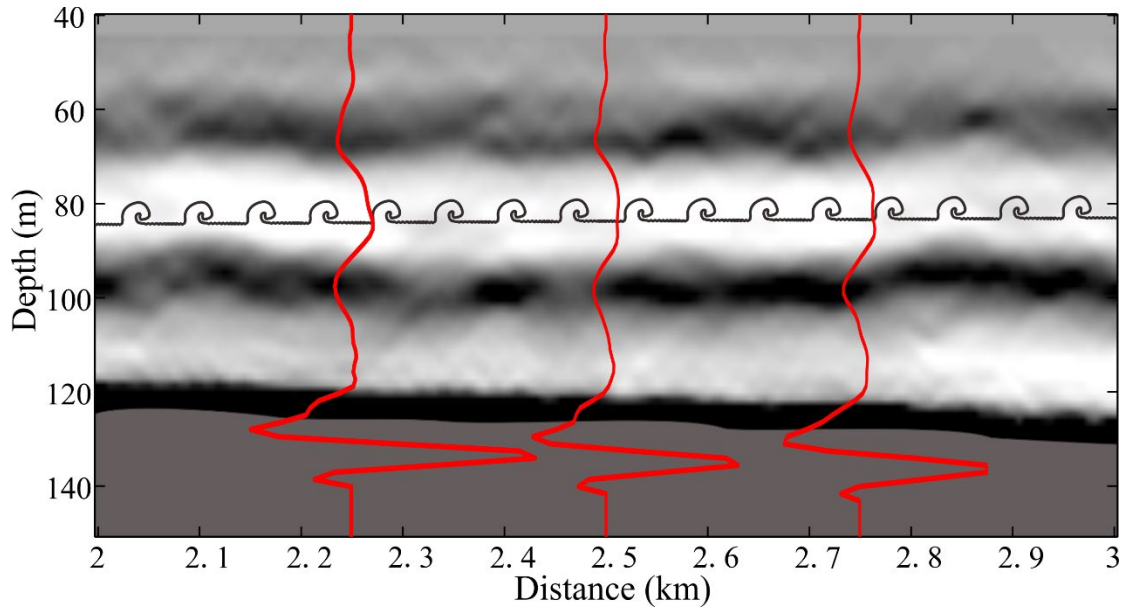
447 When there is a significant impedance difference in the water column, a reflection seismic event
 448 will occur (Holbrook et al., 2003; Ruddick et al., 2009). The impedance difference in the ocean is
 449 contributed by temperature gradient and salinity gradient, where the former is usually greater than
 450 the latter (Ruddick et al., 2009; Sallarès et al., 2009). Density is a function of temperature and
 451 salinity, so the reflection seismic events are related to density gradient. The enhanced mixing reflects
 452 the structure of density gradient, thereby changing the appearance of the reflection seismic events.
 453 Understanding the relation between diffusivity and reflection seismic events can help us analyze
 454 the spatial distribution of diapycnal mixing. Figure 8 shows that the reflection seismic event in the
 455 high diffusivity region is obviously different from that in the low diffusivity region. In the high
 456 diffusivity area (red in Figure 8), the reflection seismic events are fuzzy, discontinuous or bifurcate.
 457 While in the low diffusivity area (yellow and blue in Figure 8), the reflection seismic events are
 458 clear and continuous. This is because regions with high diffusivity are strongly mixed. The density

459 gradient is smeared by mixing, so that it affects the appearance of reflection seismic events. For
460 example, in the polarity reversal region of three seismic sections, the diffusivity is high, and the
461 reflection seismic events are fuzzy and discontinuous. Especially in the range of 5-10 km in Fig. 8c,
462 the events are obviously broken and weak. The diffusivity is low in areas where the events are clear,
463 such as the region near the seafloor around 45-50 km and the region near the sea floor around 93-
464 99 km in Figure 8a, and the region near the sea floor around 24-27 km in Figure 8c.

465

466 The diffusivity is not only related to the continuity of the reflection events, but also related to the
467 fluctuation intensity of the events. The greater the fluctuation intensity of the events, the higher the
468 spectral energy, and the greater the diffusivity value. There is a mode-1 depression internal solitary
469 wave at 50-58 km in Figure 8a, and the reflection seismic event is clear and continuous at 180 m.
470 But the diffusivity is high, because the reflection events fluctuate more strongly. It can be seen from
471 the figure that, in addition to the amplitude of the internal solitary wave, there are also many high-
472 frequency waves at the shoulders of the internal solitary wave. These waves increase the spectral
473 energy and result in a higher diffusivity. In addition, the reflection seismic events before 4 km in
474 Figure 8b is continuous and without obvious fluctuations, but the diffusivity is higher. It can be seen
475 from the figure that the reflection events of this region are thicker than that of other regions. The
476 seismic data processing of the three sections in Figure 8 is the same, so the thicker events in Figure
477 8b do not stem from the low frequency of seismic waves. We think this may be caused by small-
478 scale mixing between layers, such as K-H instability. Figure 9 is an enlarged view of 2-3 km in the
479 seismic section of L2 (Figure 5b). The wavelength of the seismic wave (red line) at 80 m is larger
480 than that at the seafloor, which is formed by the overlap of multiple wavelets. It can be seen from
481 the figure that a weak reflection event is barely visible at 80 m, which indicates a thin reflection
482 layer with weak impedance differences. The K-H instability can last for a long distance in the lateral
483 direction (Seim and Gregg, 1994; Haren et al., 2014; Chang et al., 2016; Tu et al., 2019) and enhance
484 local ocean mixing. This structure can form at the tail of internal solitary wave (Moum et al., 2003).
485 The vertical scale of the K-H instability is small and usually appears on the isopycnal. On one hand,
486 K-H instability weakens the density gradient so that the reflected seismic wave energy is reduced.
487 On the other hand, the vertical scale of K-H instability is lower than the seismic wave resolution (a
488 quarter of the seismic wave wavelength), so it causes overlapped wavelets and stretched wavelength
489 (Figure 9). Therefore, the reflection event in this area is thicker. Besides, the horizontal scale of the
490 K-H instability train is large, which may explain the larger turbulence subrange on the horizontal
491 slope spectrum (Figure 7b).

492



493
494 Figure 9. Schematic of the K-H instability. The red lines are the seismic waves, and the black billows
495 represent the K-H instability.

496
497 **4.2 Enhanced diapycnal mixing induced by the polarity reversal of internal solitary waves**

498
499 Strong mixing in the ocean mainly occurs near rough topography or area with strong tides (Simpson
500 et al., 1996; Rippeth et al., 2001, 2003; Nash and Moum, 2001; Klymak et al., 2008; Jarosz et al.,
501 2013; Staalstrøm et al., 2015; Wijesekera et al., 2020; Voet et al., 2020). The Dongsha Atoll region
502 in the South China Sea possesses both features. On one hand, the Dongsha Atoll lies on the
503 continental slope with variable topography. On the other hand, large-amplitude internal solitary
504 waves (Alford et al., 2015) propagating from the Luzon Strait reflect, refract, and shoal in this region.
505 This process will dissipate most of the energy carried by the internal solitary waves. Especially in
506 the shoaling process, polarity reversal and breaking occur and the energy of internal solitary waves
507 transfer to smaller-scale waves. Our results (Figure 6) indicate that the average diffusivity has the
508 magnitude order of $O(10^{-4})$ - $O(10^{-3}) \text{ m}^2 \text{ s}^{-1}$, consistent with previous observations by other techniques.
509 St. Laurent (2008) observed turbulent mixing on the continental shelf and slope, and found that the
510 mixing is higher at the shelf break, and the magnitude order of average dissipation is $O(10^{-7})$ - $O(10^{-$

511 $6) \text{ m}^2 \text{ s}^{-1}$. According to the average buoyancy frequency $N = 6cph$, the magnitude order of the
512 average diffusivity is $O(10^{-4})$ - $O(10^{-3}) \text{ m}^2 \text{ s}^{-1}$ and consistent with our result. Yang et al. (2014)
513 observed diapycnal mixing on the continental shelf and slope, and found that the average diffusivity
514 can reach $O(10^{-3}) \text{ m}^2 \text{ s}^{-1}$ too. Similar results have been reported in the study of internal solitary
515 waves shoaling in other regions. For example, Sandstrom et al. (1989) observed the turbulent
516 diffusivity caused by the nonlinear internal wave group on the continental slope of Canada, and
517 found the average diffusivity of $2.4 \times 10^{-3} \text{ m}^2 \text{ s}^{-1}$. Carter et al. (2005) observed the elevation internal
518 solitary waves in Monterey Bay and a diffusivity on the magnitude order of $O(10^{-4}) \text{ m}^2 \text{ s}^{-1}$. Richards
519 et al. (2013) observed the shoaling of nonlinear internal waves at the St. Lawrence Estuary, which
520 induced high turbulence and enhanced mixing. Therefore, it is reasonable that diapycnal mixing
521 induced by nonlinear internal waves on the continental shelf and slope in the northern South China

522 Sea can reach 100 times that in the open ocean.

523

524 The high diffusivity is mainly in the leading internal solitary wave during the polarity reversal. We
525 suggest that strong mixing may be caused by internal wave breaking due to convective instability.
526 In Figures 8a and 8c, the reflection seismic events are obviously discontinuous in the high
527 turbulence area, indicating that the density gradient is weakened by internal wave breaking. The
528 trough of the internal solitary wave decelerates first when the polarity is reversed (Shroyer et al.,
529 2008), which makes the Froude number (Fr) greater than 1 and causes convective instability. This
530 phenomenon can be found in other observational data. In the high-frequency acoustic section, the
531 backscatter at the top of internal solitary wave is increased when it changes from depression to
532 elevation wave (Orr and Mignerey, 2003), which indicates that the turbulence of the front increased.
533 However, in the seismic section of Figure 8b, we did not find breaking at the front the polarity
534 reversal internal solitary wave. The strong mixing of this internal solitary wave may be induced by
535 shear instability (Figure 9). Therefore, both convective instability and shear instability are
536 responsible for the enhanced mixing in this process. In addition, the non-polarity reversal region in
537 Figure 8a has a higher diffusivity in 50-150 m than other regions. This range is in the thermocline
538 (Figure 1c). The internal waves usually greatly increase mixing in the thermocline, which is related
539 to shear instability of internal waves (Mackinnon and Gregg, 2003). Shear instability is an important
540 mechanism of internal wave dissipation (Farmer and Smith, 1978), and it more likely occurs in
541 nonlinear internal waves than convective instability (Zhang and Alford, 2014). The results of high-
542 frequency acoustic observations show that the enhanced backscatter at the bottom of the thermocline
543 represents higher shear instability when the internal solitary waves are shoaling (Orr and Mignerey,
544 2003), which is consistent with the depth range of high diffusivity in our results.

545

546 What is inconsistent with the observed distribution of mixing is that our results do not show
547 diffusivity in the bottom boundary layer. Because our seismic data was collected in summer, the
548 strong stratification at this time limits the vertical range of the bottom boundary layer (Mackinnon
549 and Gregg, 2003). So that the bottom boundary layer near the Dongsha Atoll is thin and lower than
550 the thickness that can be recorded by seismic data. So, the diffusivity we calculated does not include
551 the bottom boundary layer. The enhanced diapycnal mixing induced by the polarity reversal of
552 internal solitary waves plays an important role in local environment and primary productivity. On
553 one hand, diapycnal mixing on the continental slope and shelf makes an important contribution to
554 ocean heat flux, which affects climate and the ocean through heat exchange of local water column
555 (Rahmstorf, 2003; Tian et al., 2009). On the other hand, the vertical flux caused by turbulence can
556 redistribute materials in the ocean and have an important impact on the marine ecological
557 environment (Sharples et al., 2001; Moum et al., 2003; Klymak and Moum, 2003; Wang et al., 2007).

558

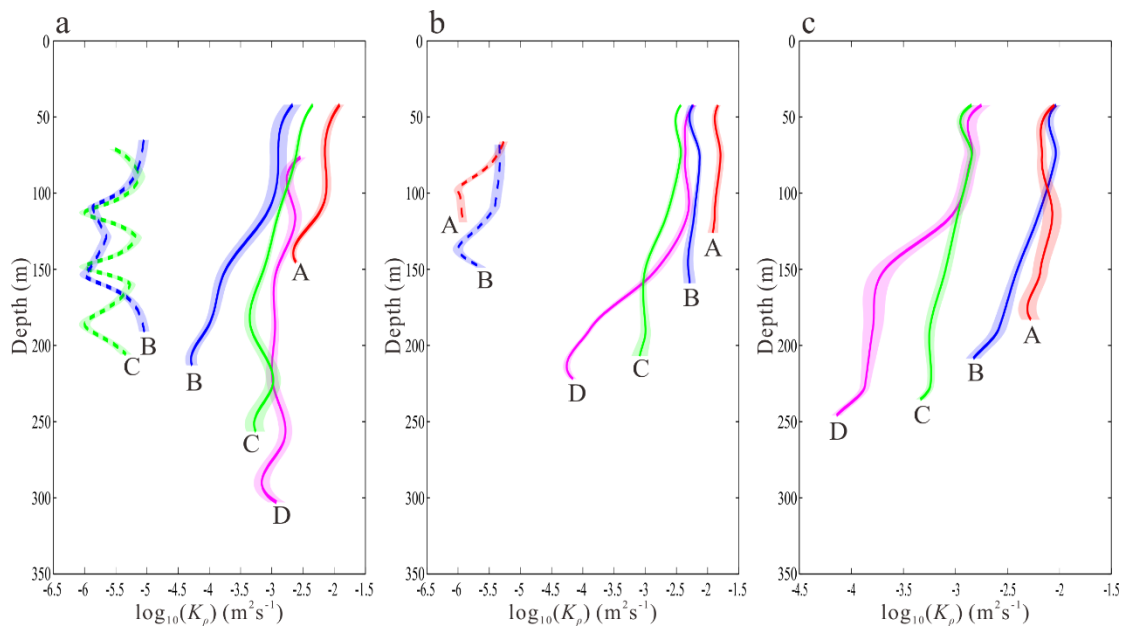
559 **4.3 The mixing scheme of internal solitary wave shoaling**

560

561 We compared the vertical distribution of diffusivity with the vertical mixing scheme of internal
562 wave breaking proposed by Vlasenko and Hutter (2002). Although Klymak and Legg (2010) also
563 proposed a mixing scheme for internal wave shoaling and achieved good results in numerical
564 simulation, we cannot use that method to calculate mixing parameters because of lacking high
565 resolution density observation data. Figure 10 shows the vertical distribution of diffusivity from

566 seismic data (solid line) and the diffusivity calculated from mixing scheme (dashed line) at 4
567 positions of the three survey lines (black arrows in Figure 8). The reflection events in the L3 section
568 are broken, and it cannot be guaranteed that the events are parallel to the streamline. Therefore, we
569 did not use the method described in section 2.3 to calculate the wave-induced velocity, and thus did
570 not obtain the diffusivity of the mixing scheme. It can be seen from Figure 10 that the turbulent
571 diffusivity gradually decreases from shallow to deep water. Except for the local low diffusivity value
572 in the deep water at the position D of Figure 10b and 10c, the diffusivity reduction rate at other
573 locations is similar. Figures 10a and 10b show that the parameterized diffusivity is nearly 2--3 orders
574 of magnitude smaller than our result, but they have a similar trend of change. In Figure 10a (line
575 L1), the parameterized diffusivity (blue dotted line) at position B decreases by an order of magnitude
576 within 50-100 m. This tendency is same as our results. However, the parameterized diffusivity
577 within 150-200 m increases by one order of magnitude, which is inconsistent with our results (solid
578 blue line). The parameterized diffusivity at position C fluctuates and keeps a decreasing trend on
579 the whole. In the survey line L2, we selected position A and position B to calculate the parameterized
580 diffusivity. The diffusivity at position A (red dashed line) decreases rapidly within 60-100 m, and
581 then almost keeps unchanged. This is different from our result (solid red line), and the reduction
582 rate of the diffusivity is larger than our result. The trend of the diffusivity at position B (blue dashed
583 line) above 110 m is consistent with our results (solid blue line), but the diffusivity below 110 m
584 decreases rapidly and then rises again. In our results, the diffusivity decreases slowly at the same
585 depth. The value is consistent with that in the open ocean. However, the mixing enhanced obviously
586 on the continental shelf and slope, because of the internal wave shoaling. The mixing scheme
587 underestimates mixing, especially the strong mixing induced by the polarity reversal of internal
588 solitary waves. Our results indicate that near the Dongsha Atoll, where large-amplitude internal
589 solitary waves develop, mixing will be enhanced by the shoaling internal solitary waves. The
590 diffusivity gradually decreases from shallow to deep water (not including the bottom boundary
591 layer). This has important implications for improving the mixing scheme for models on the
592 continental shelf and slope.

593



594

595

Figure 10. The vertical distribution of diffusivity from seismic data compare with the mixing scheme.

596 The solid line represents the vertical distribution of diffusivity at the four positions A (red), B (blue), C
597 (green) and D (magenta), and the dotted line represents the parameterized diffusivity at the corresponding
598 positions. The shadow indicates the margin of errors.

599

600 **5. Conclusions**

601

602 We have observed the polarity reversal of internal solitary waves by reflection seismic data near the
603 Dongsha Atoll in the South China Sea, and calculated their slope spectra (Figure 6) and diapycnal
604 diffusivity (Figure 8). The results show that the average diapycnal diffusivities of the three survey
605 lines are about two orders of magnitude greater than the open-ocean value. We calculated the
606 average spectral slope of the polarity reversal and non-polarity-reversal regions (Figure 7), and
607 found that the former is about 3 times larger than the latter. The diffusivity maps reveal that
608 horizontally high diffusivity is mainly in the leading wavefront of an internal solitary wave in
609 reversing polarity, and vertically high diffusivity is mainly in the thermocline (50-100 m).

610

611 We analyzed the relation between reflection seismic events and diapycnal diffusivity. The result
612 indicates that continuous and clear reflection events correspond to low diffusivity, while
613 discontinuous or fuzzy events correspond to high diffusivity. The strength of the events also affects
614 the magnitude of diffusivity. The stronger the fluctuation, the higher the spectral energy, and the
615 higher the diffusivity. In addition, we observed an area of high diffusivity with a large horizontal
616 scale in L2, and the reflection events did not appear to be discontinuous or fuzzy. We suggest that
617 this enhanced mixing may be induced by the K-H instability (Figure 9). The vertical scale of the K-
618 H instability is smaller than the resolution of our seismic data, so we cannot observe clearly in the
619 seismic data. But its high-energy characteristics can be recorded by reflection events.

620

621 Our results show that shoaling internal solitary waves enhance local mixing. The magnitude order
622 of diapycnal diffusivity is consistent with previous studies. We suggest that there are two
623 mechanisms that could account for the enhanced mixing. On one hand, the polarity reversal of
624 internal solitary waves results in convection instability, which induces internal solitary wave
625 breaking. This mechanism appears at the leading edge of one internal solitary wave in the survey
626 lines L1 and L3. The discontinuous reflection events indicate that the internal solitary wave is
627 broken. While in the seismic section of L2, the reflection events are continuous and clear at the
628 leading edge of the internal solitary wave and other strong mixing areas in the three sections. Such
629 strong mixing may be caused by shear instability.

630

631 We picked four positions from the diffusivity maps to analyze the vertical distribution of diapycnal
632 diffusivity (Figure 10). Our result shows that the diffusivity gradually decreased from shallow to
633 deep water (excluding the bottom boundary layer). Compared with previous one mixing scheme,
634 the parameterized diffusivity is about 2-3 orders of magnitude smaller. This means that the mixing
635 scheme underestimates mixing induced by internal solitary wave shoaling near the Dongsha Atoll.
636 However, the vertical pattern of the parameterized diffusivity is consistent with our result.

637

638 **Appendix:** The uncertainty of diffusivity from seismic data

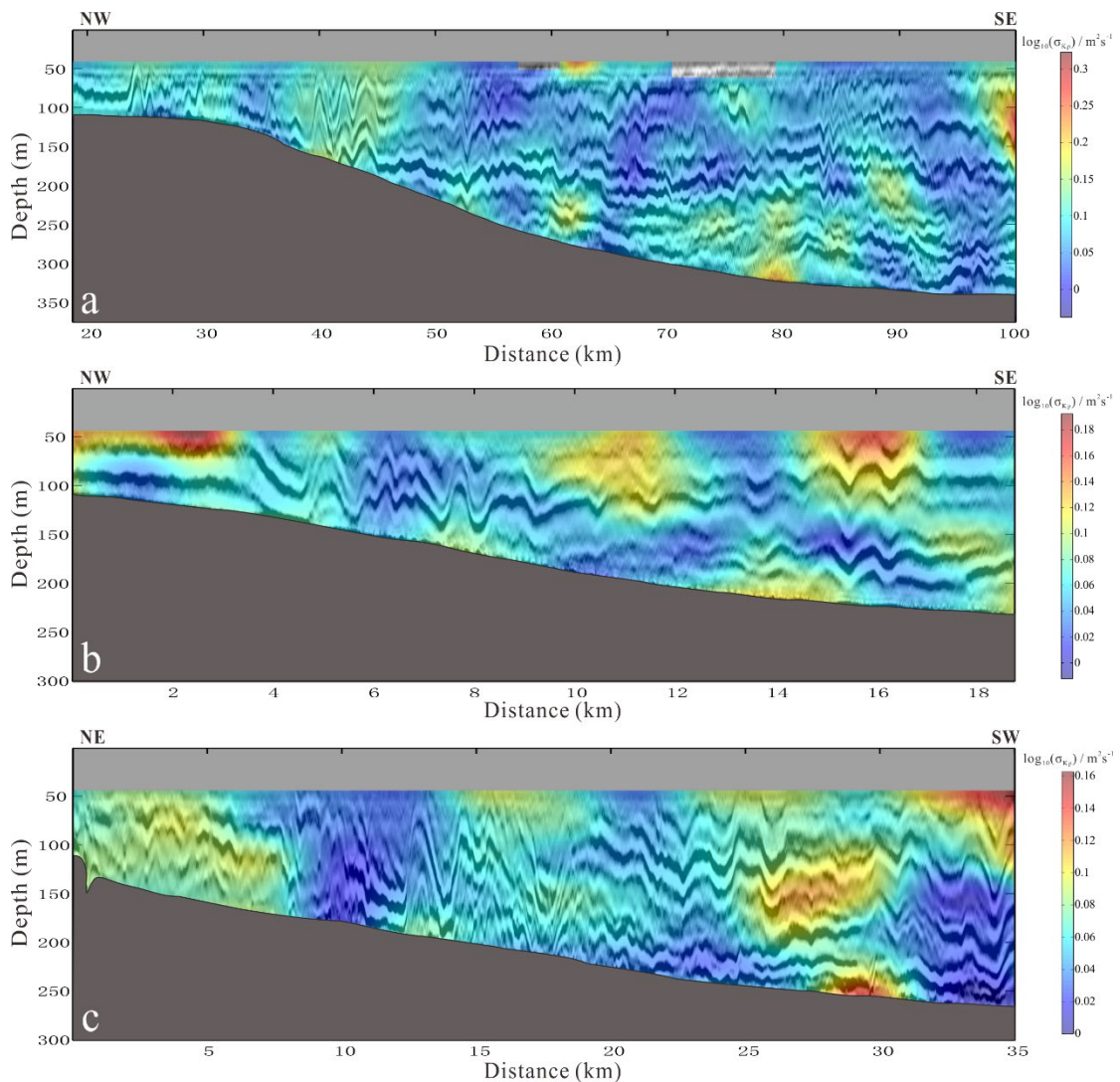
639

640 According to formulas 2-1 and 2-2, the parameters used in calculating diffusivity are buoyancy
 641 frequency (N), mixing coefficient (K), and the Kolmogorov constant (C_T). It can be seen from the
 642 formula that the diffusivity is proportional to N . The mean deviation of N we used is about 2%
 643 (Figure 1), so the uncertainty of the corresponding diffusion rate is about 0.008 logarithmic units.
 644 In addition, diffusivity is proportional to $K^{-1/2}$, which is 0.1-0.4 (Mashayek et al., 2017), so the
 645 corresponding uncertainty of diffusivity is about 0.15 logarithmic units. Similarly, diffusivity is
 646 proportional to $C_T^{-3/2}$. The value of C_T is 0.3-0.5 (Sreenivasan, 1996), and the corresponding
 647 diffusivity uncertainty is about 0.15.

648

649 In addition, the key reason for the uncertainty of diffusivity in our calculation is the fitting of the
 650 Batchelor model and the slope spectrum (Figure 3b and Figure 6). We evaluated the uncertainty
 651 based on the least squares standard deviation between the Batchelor model and the slope spectrum.
 652 The uncertainty of the three diffusivity maps in Figure 8 is shown in Figure A1.

653



654

655 Figure A1. The diffusivity uncertainty along survey lines L1 (a), L2 (b) and L3 (c).

656

657 **Code and data availability.** The bathymetry data were provided by the General Bathymetric
 658 Chart of the Oceans (GEBCO, <http://www.gebco.net/>), and prepared using the Generic Mapping

659 Tools (GMT, <https://generic-mapping-tools.org/>). The hydrological data set we used were product
660 by Copernicus Marine Environment Monitoring Service (CMEMS,
661 <https://resources.marine.copernicus.eu/>). The seismic data were processed using Seismic Unix
662 (<https://wiki.seismic-unix.org/start/>).

663

664 **Author contribution.** The concept of this study was developed by Haibin Song and extended
665 upon by all involved. Yi Gong implemented the study and performed the analysis with guidance
666 from Haibin Song, Zhongxiang Zhao, Yongxian Guan, Kun Zhang, Yunyan Kuang and Wenhao Fan
667 collaborated in discussing the results and composing the manuscript.

668

669 **Competing interests.** The authors declare that they have no conflict of interest.

670

671 **Acknowledgements.** The seismic data own to the Guangzhou Marine Geological Survey
672 (GMGS). Thanks to the GMGS for providing 2D seismic data. This work is supported by the
673 National Natural Science Foundation of China (Grant Number 41976048); and the National Key
674 R&D Program of China (2018YFC0310000).

675

676 **References**

- 677 Aghsaee, P., Boegman, L., and Lamb, K. G.: Breaking of shoaling internal solitary waves, *Journal of*
678 *Fluid Mechanics*, 659, 289-317, <https://doi.org/10.1017/S002211201000248X>, 2010.
- 679 Alford, M. H., Peacock, T., MacKinnon, J. A., Nash, J. D., Buijsman, M. C., Centurioni, L. R., Chao, S.
680 -Y., Chang, M. -H., Farmer, D. M., Fringer, O. B., Fu, K. -H., Gallacher, P. C., Graber, H. C.,
681 Helfrich, K. R., Jachec, S. M., Jackson, C. R., Klymak, J. M., Ko, D. S., Jan, S., Shaun Johnston, T.
682 M., Legg, S., Lee, I. -H., Lien, R. -C., Mercier, M. J., Moum, J. N., Musgrave, R., Park, J. -H.,
683 Pickering, A. I., Pinkel, R., Rainville, L., Ramp, S. R., Rudnick, D. L., Sarkar, S., Scotti, A.,
684 Simmons, H. L., St Laurent, L. C., Venayagamoorthy, S. K., Wang, Y. -H., Wang, J., Yang, Y. J.,
685 Paluszkiwicz, T., and Tang, T. -Y.: The formation and fate of internal waves in the South China Sea,
686 *Nature*, 521, 65-69, <https://doi.org/10.1038/nature14399>, 2015. Bai, Y., Song, H., Guan, Y., and Yang,
687 S.: Estimating depth of polarity conversion of shoaling internal solitary waves in the northeastern
688 South China Sea, *Continental Shelf Research*, 143, 9-17, <https://doi.org/10.1016/j.csr.2017.05.014>,
689 2017.
- 690 Bogucki, D., Dickey, T., and Redekopp, L. G.: Sediment resuspension and mixing by resonantly
691 generated internal solitary waves, *Journal of Physical Oceanography*, 27, 1181-1196,
692 [https://doi.org/10.1175/1520-0485\(1997\)027<1181:SRAMBR>2.0.CO;2](https://doi.org/10.1175/1520-0485(1997)027<1181:SRAMBR>2.0.CO;2), 1997.
- 693 Bourgault, D., Blokhina, M. D., Mirshak, R., and Kelley, D. E.: Evolution of a shoaling internal
694 solitary wavetrain, *Geophysical Research Letters*, 34, <https://doi.org/10.1029/2006gl028462>, 2007.
- 695 Cai, S., Xie, J., and He, J.: An overview of internal solitary waves in the South China Sea, *Surveys in*
696 *Geophysics*, 33, 927-943, <https://doi.org/10.1007/s10712-012-9176-0>, 2012.
- 697 Carter, G. S., Gregg, M. C., and Lien, R. -C.: Internal waves, solitary-like waves, and mixing on the
698 Monterey Bay shelf, *Continental Shelf Research*, 25, 1499-1520,
699 <https://doi.org/10.1016/j.csr.2005.04.011>, 2005.
- 700 Chang, M.-H., Jheng, S.-Y., and Lien, R.-C.: Trains of large Kelvin-Helmholtz billows observed in the
701 Kuroshio above a seamount, *Geophysical Research Letters*, 43, 8654-8661,
702 <https://doi.org/10.1002/2016gl069462>, 2016.

703 Chang, M.-H., Lien, R.-C., Tang, T. Y., D'Asaro, E. A., and Yang, Y. J.: Energy flux of nonlinear
704 internal waves in northern South China Sea, *Geophysical Research Letters*, 33,
705 <https://doi.org/10.1029/2005gl025196>, 2006.

706 Dickinson, A., White, N. J., and Caulfield, C. P.: Spatial variation of diapycnal diffusivity estimated
707 from seismic imaging of internal wave field, Gulf of Mexico, *Journal of Geophysical Research:*
708 *Oceans*, 122, 9827-9854, <https://doi.org/10.1002/2017jc013352>, 2017.

709 Fan, W., Song, H., Gong, Y., Sun, S., Zhang, K., Wu, D., Kuang, Y., and Yang, S.: The shoaling mode-2
710 internal solitary waves in the Pacific coast of Central America investigated by marine seismic survey
711 data, *Continental Shelf Research*, 212, 104318, <https://doi.org/10.1016/j.csr.2020.104318>, 2021.

712 Fortin, W. F. J., Holbrook, W. S., and Schmitt, R. W.: Mapping turbulent diffusivity associated with
713 oceanic internal lee waves offshore Costa Rica, *Ocean Science*, 12, 601-612,
714 <https://doi.org/10.5194/os-12-601-2016>, 2016.

715 Gregg, M. C. and Özsoy, E.: Mixing on the Black Sea Shelf north of the Bosphorus, *Geophysical*
716 *Research Letters*, 26, 1869-1872, <https://doi.org/10.1029/1999gl900431>, 1999.

717 Grimshaw, R., Pelinovsky, E., Talipova, T., and Kurkina, O.: Internal solitary waves: propagation,
718 deformation and disintegration, *Nonlinear Processes in Geophysics*, 17, 633-649,
719 <https://doi.org/10.5194/npg-17-633-2010>, 2010.

720 Haren, H. v., Gostiaux, L., Morozov, E., and Tarakanov, R.: Extremely long Kelvin-Helmholtz billow
721 trains in the Romanche Fracture Zone, *Geophysical Research Letters*, 41, 8445-8451,
722 <https://doi.org/10.1002/2014GL062421>, 2014.

723 Holbrook, W. S., Pa'ramo, P., Pearse, S., and Schmitt, R. W.: Thermohaline fine structure in an
724 oceanographic front from seismic reflection profiling, *Science*, 301, 821-824,
725 <https://doi.org/10.1126/science.1085116>, 2003.

726 Holbrook, W. S., Fer, I., Schmitt, R. W., Lizarralde, D., Klymak, J. M., Helfrich, L. C., and Kubichek,
727 R.: Estimating oceanic turbulence dissipation from seismic images, *Journal of Atmospheric and*
728 *Oceanic Technology*, 30, 1767-1788, <https://doi.org/10.1175/jtech-d-12-00140.1>, 2013.

729 Holloway, P. E.: A regional model of the semidiurnal internal tide on the Australian North West Shelf,
730 *Journal of Geophysical Research: Oceans*, 106, 19625-19638, <https://doi.org/10.1029/2000jc000675>,
731 2001.

732 Holloway, P. E., Pelinovsky, E., and Talipova, T.: A generalized Korteweg-de Vries model of internal
733 tide transformation in the coastal zone, *Journal of Geophysical Research: Oceans*, 104, 18333-
734 18350, <https://doi.org/10.1029/1999jc900144>, 1999.

735 Jan, S., Chern, C-S., Wang, J., and Chiou, M-D.: Generation and propagation of baroclinic tides
736 modified by the Kuroshio in the Luzon Strait, *Journal of Geophysical Research*, 117, C02019,
737 <https://doi.org/10.1029/2011JC007229>, 2012.

738 Jarosz, E., Teague, W. J., Book, J. W., and Beşiktepe, Ş. T.: Observed volume fluxes and mixing in the
739 Dardanelles Strait, *Journal of Geophysical Research: Oceans*, 118, 5007-5021,
740 <https://doi.org/10.1002/jgrc.20396>, 2013.

741 Klymak, J. M. and Legg, S. M.: A simple mixing scheme for models that resolve breaking internal
742 waves, *Ocean Modelling*, 33, 224-234, <https://doi.org/10.1016/j.ocemod.2010.02.005>, 2010.

743 Klymak, J. M. and Moum, J. N.: Internal solitary waves of elevation advancing on a shoaling shelf,
744 *Geophysical Research Letters*, 30, n/a-n/a, <https://doi.org/10.1029/2003gl017706>, 2003.

745 Klymak, J. M. and Moum, J. N.: Oceanic isopycnal slope spectra. Part II: Turbulence, *Journal of*
746 *Physical Oceanography*, 37, 1232-1245, <https://doi.org/10.1175/jpo3074.1>, 2007.

747 Klymak, J. M., Pinkel, R., and Rainville, L.: Direct breaking of the internal tide near topography:
748 Kaena Ridge, Hawaii, *Journal of Physical Oceanography*, 38, 380-399,
749 <https://doi.org/10.1175/2007jpo3728.1>, 2008.

750 Klymak, J. M., Pinkel, R., Liu, C.-T., Liu, A. K., and David, L.: Prototypical solitons in the South
751 China Sea, *Geophysical Research Letters*, 33, <https://doi.org/10.1029/2006gl025932>, 2006.

752 Kunze, E.: Internal-wave-driven mixing: global geography and budgets, *Journal of Physical*
753 *Oceanography*, 47, 1325-1345, <https://doi.org/10.1175/jpo-d-16-0141.1>, 2017.

754 Lee, C. M., Sanford, T. B., Naveira Garabato, A. C., Waterman, S., Fer, I., Carter, G. S., Huussen, T. N.,
755 Whalen, C. B., Talley, L. D., Pinkel, R., Sun, O. M., St. Laurent, L. C., Polzin, K. L., Simmons, H.
756 L., Kunze, E., Alford, M. H., Nash, J. D., MacKinnon, J. A., and Waterhouse, A. F.: Global patterns
757 of diapycnal mixing from measurements of the turbulent dissipation rate, *Journal of Physical*
758 *Oceanography*, 44, 1854-1872, <https://doi.org/10.1175/jpo-d-13-0104.1>, 2014.

759 Lien, R. C., Tang, T. Y., Chang, M. H., and D'Asaro, E. A.: Energy of nonlinear internal waves in the
760 South China Sea, *Geophysical Research Letters*, 32, <https://doi.org/10.1029/2004gl022012>, 2005.

761 Liu, A. K., Chang, Y. S., Hsu, M.-K., and Liang, N. K.: Evolution of nonlinear internal waves in the
762 East and South China Seas, *Journal of Geophysical Research: Oceans*, 103, 7995-8008,
763 <https://doi.org/10.1029/97jc01918>, 1998.

764 MacKinnon, J. A. and Gregg, M. C.: Mixing on the late-summer new England shelf—solibores, shear,
765 and stratification, *Journal of Physical Oceanography*, 33, 1476-1492, [https://doi.org/10.1175/1520-0485\(2003\)033<1476:MOTLNE>2.0.CO;2](https://doi.org/10.1175/1520-0485(2003)033<1476:MOTLNE>2.0.CO;2), 2003.

767 Mashayek, A., Salehipour, H., Bouffard, D., Caulfield, C. P., Ferrari, R., Nikurashin, M., Peltier, W. R.,
768 and Smyth, W. D.: Efficiency of turbulent mixing in the abyssal ocean circulation, *Geophysical*
769 *Research Letters*, 44, 6296-6306, <https://doi.org/10.1002/2016GL072452>, 2017.

770 Masunaga, E., Arthur, R. S., and Fringer, O. B.: Internal wave breaking dynamics and associated
771 mixing in the Coastal Ocean, *encyclopedia of Ocean Science*, 3rd edn. Academic Press, Cambridge,
772 548-554, <https://doi.org/10.1016/b978-0-12-409548-9.10953-4>, 2019.

773 Min, W., Li, Q., Zhang, P., Xu, Z., and Yin, B.: Generation and evolution of internal solitary waves in
774 the southern Taiwan Strait, *Geophysical & Astrophysical Fluid Dynamics*, 13:3, 287-302,
775 <https://doi.org/10.1080/03091929.2019.1590568>, 2019.

776 Mojica, J. F., Sallarès, V., and Biescas, B.: High-resolution diapycnal mixing map of the Alboran Sea
777 thermocline from seismic reflection images, *Ocean Science*, 14, 403-415, <https://doi.org/10.5194/os-14-403-2018>, 2018.

779 Moum, J., N, Farmer, D., M, Smyth, W., D, Armi, L., and Vagle, S.: Structure and generation of
780 turbulence at interfaces strained by internal solitary waves propagating shoreward over the
781 continental shelf, *Journal of Physical Oceanography*, 33, 2093-2112, [https://doi.org/10.1175/1520-0485\(2003\)033<2093:SAGOTA>2.0.CO;2](https://doi.org/10.1175/1520-0485(2003)033<2093:SAGOTA>2.0.CO;2), 2003.

783 Moum, J. N., Farmer, D. M., Shroyer, E. L., Smyth, W. D., and Armi, L.: Dissipative losses in
784 nonlinear internal waves propagating across the Continental Shelf, *Journal of Physical*
785 *Oceanography*, 37, 1989-1995, <https://doi.org/10.1175/jpo3091.1>, 2007a.

786 Moum, J. N., Klymak, J. M., Nash, J. D., Perlin, A., and Smyth, W. D.: Energy transport by nonlinear
787 internal waves, *Journal of Physical Oceanography*, 37, 1968-1988, <https://doi.org/10.1175/jpo3094.1>,
788 2007b.

789 Nakamura, Y., Noguchi, T., Tsuji, T., Itoh, S., Niino, H., and Matsuoka, T.: Simultaneous seismic
790 reflection and physical oceanographic observations of oceanic fine structure in the Kuroshio

791 extension front, *Geophysical Research Letters*, 33, <https://doi.org/10.1029/2006gl027437>, 2006.

792 Nandi, P., Holbrook, W. S., Pearse, S., Páramo, P., and Schmitt, R. W.: Seismic reflection imaging of
793 water mass boundaries in the Norwegian Sea, *Geophysical Research Letters*, 31, 345-357,
794 <https://doi.org/10.1029/2004GL021325>, 2004.

795 Nash, J. D. and Moun, J. N.: Internal hydraulic flows on the continental shelf High drag states over a
796 small bank, *Journal of Geophysical Research*, 106, 4593-4611,
797 <https://doi.org/10.1029/1999JC000183>, 2001.

798 Orr, M. H. and Mignerey, P. C.: Nonlinear internal waves in the South China Sea: Observation of the
799 conversion of depression internal waves to elevation internal waves, *Journal of Geophysical*
800 *Research*, 108, <https://doi.org/10.1029/2001jc001163>, 2003.

801 Osborn, T. R.: Estimates of the local rate of vertical diffusion from dissipation measurements, *Journal*
802 *of Physical Oceanography*, 10, 83-89, [https://doi.org/10.1175/1520-0485\(1980\)010<0083:Eotlro>2.0.Co;2](https://doi.org/10.1175/1520-0485(1980)010<0083:Eotlro>2.0.Co;2), 1980.

804 Pacanowski, R. and Philander, S.: Parameterization of vertical mixing in numerical models of tropical
805 oceans, *Journal of Physical Oceanography*, 11, 1443-1451, [https://doi.org/10.1175/1520-0485\(1981\)011<1443:povmin>2.0.co;2](https://doi.org/10.1175/1520-0485(1981)011<1443:povmin>2.0.co;2), 1981.

807 Palmer, M. R., Inall, M. E., and Sharples, J.: The physical oceanography of Jones Bank: A mixing
808 hotspot in the Celtic Sea, *Progress in Oceanography*, 117, 9-24,
809 <https://doi.org/10.1016/j.pocean.2013.06.009>, 2013.

810 Park, J.-H., and Farmer, D.: Effects of Kuroshio intrusions on nonlinear internal waves in the South
811 China Sea during winter, *Journal of Geophysical Research: Oceans*, 118, 7081-7094,
812 <https://doi.org/10.1002/2013JC008983>, 2013.

813 Ramhstorf, S.: Thermohaline circulation: The current climate, *Nature*, 421, 699,
814 <https://doi.org/10.1038/421699a>, 2003.

815 Richards, C., Bourgault, D., Galbraith, P. S., Hay, A., and Kelley, D. E.: Measurements of shoaling
816 internal waves and turbulence in an estuary, *Journal of Geophysical Research: Oceans*, 118, 273-286,
817 <https://doi.org/10.1029/2012jc008154>, 2013.

818 Rippeth, T. P., Fisher, N. R., and Simpson, J. H.: The cycle of turbulent dissipation in the presence of
819 tidal straining, *Journal of Physical Oceanography*, 31, 2458-2471, [https://doi.org/10.1175/1520-0485\(2001\)031<2458:TCOTDI>2.0.CO;2](https://doi.org/10.1175/1520-0485(2001)031<2458:TCOTDI>2.0.CO;2), 2001.

821 Rippeth, T. P., Simpson, J. H., Williams, E., and Inall, M. E.: Measurement of the rates of production
822 and dissipation of turbulent kinetic energy in an energetic tidal flow Red Wharf Bay revisited,
823 *Journal of Physical Oceanography*, 33, 1889-1901, [https://doi.org/10.1175/1520-0485\(2003\)033<1889:MOTROP>2.0.CO;2](https://doi.org/10.1175/1520-0485(2003)033<1889:MOTROP>2.0.CO;2), 2003.

825 Ruddick, B., Song, H., Dong, C., and Pinheiro, L.: Water column seismic images as maps of
826 temperature gradient, *Oceanography*, 21, 192-205, <https://doi.org/10.5670/oceanog.2009.19>, 2009.

827 Sallarès, V., Mojica, J. F., Biescas, B., Klaeschen, D., and Gràcia, E.: Characterization of the
828 submesoscale energy cascade in the Alboran Sea thermocline from spectral analysis of high-
829 resolution MCS data, *Geophysical Research Letters*, 43, 6461-6468,
830 <https://doi.org/10.1002/2016GL069782>, 2016.

831 Sallarès, V., Biescas, B., Buffett, G., Carbonell, R., Dañobeitia, J. J., and Pelegrí, J. L.: Relative
832 contribution of temperature and salinity to ocean acoustic reflectivity, *Geophysical Research Letters*,
833 36, <https://doi.org/10.1029/2009gl040187>, 2009.

834 Sandstrom, H. and Oakey, N. S.: Dissipation in internal tides and solitary waves, *Journal of Physical*

835 Oceanography, 25, 604-614, [https://doi.org/10.1175/1520-0485\(1995\)025<0604:DIITAS>2.0.CO;2](https://doi.org/10.1175/1520-0485(1995)025<0604:DIITAS>2.0.CO;2),
836 1995.

837 Sandstrom, H., Elliot, J. A., and Cchrane, N. A.: Observing groups of solitary internal waves and
838 turbulence with BATFISH and Echo-Sounder, *Journal of Physical Oceanography*, 19, 987-997,
839 [https://doi.org/10.1175/1520-0485\(1989\)019<0987:OGOSIW>2.0.CO;2](https://doi.org/10.1175/1520-0485(1989)019<0987:OGOSIW>2.0.CO;2), 1989.

840 Seim, H. E. and Gregg, M. C.: Detailed observations of a naturally occurring shear instability, *Journal*
841 *of Geophysical Research*, 99, 10049, <https://doi.org/10.1029/94jc00168>, 1994.

842 Sharples, J., Moore, C. M., and Abraham, E. R.: Internal tide dissipation, mixing, and vertical nitrate
843 flux at the shelf edge of NE New Zealand, *Journal of Geophysical Research: Oceans*, 106, 14069-
844 14081, <https://doi.org/10.1029/2000jc000604>, 2001.

845 Sheen, K. L., White, N. J., and Hobbs, R. W.: Estimating mixing rates from seismic images of oceanic
846 structure, *Geophysical Research Letters*, 36, <https://doi.org/10.1029/2009gl040106>, 2009.

847 Shroyer, E., L, Moum, J., N, and Nash, J., D: Observations of polarity reversal in shoaling nonlinear
848 internal waves, *Journal of Physical Oceanography*, 39, 691-701,
849 <http://dx.doi.org/10.1175/2008JPO3953.1>, 2008.

850 Simpson, J. H., Crawford, W. R., Rippeth, T. P., Campbell, A. R., and Cheok, J. V. S.: The vertical
851 structure of turbulent dissipation in shelf seas, *Journal of Physical Oceanography*, 26, 1579–1590,
852 [https://doi.org/10.1175/1520-0485\(1996\)026<1579:TVSOTD>2.0.CO;2](https://doi.org/10.1175/1520-0485(1996)026<1579:TVSOTD>2.0.CO;2), 1996.

853 Sreenivasan, K. R.: The passive scalar spectrum and the Obukhov–Corrsin constant, *Physics of Fluids*,
854 8, 189-196, <https://doi.org/10.1063/1.868826>, 1996.

855 St Laurent, L., Simmons, H., Tang, T. Y., and Wang, Y.: Turbulent properties of internal waves in the
856 South China Sea, *Oceanography*, 24, 78-87, <https://doi.org/10.5670/oceanog.2011.96>, 2011.

857 St. Laurent, L.: Turbulent dissipation on the margins of the South China Sea, *Geophysical Research*
858 *Letters*, 35, <https://doi.org/10.1029/2008gl035520>, 2008.

859 Staalstrøm, A., Arneborg, L., Liljebladh, B., and Broström, G.: Observations of turbulence caused by a
860 combination of tides and mean baroclinic flow over a Fjord Sill, *Journal of Physical Oceanography*,
861 45, 355-368, <https://doi.org/10.1175/jpo-d-13-0200.1>, 2015.

862 Terletska, K., Choi, B. H., Maderich, V., and Talipova, T.: Classification of internal waves shoaling
863 over slope-shelf topography, *Russian Journal of Earth Science*, 20,
864 <https://doi.org/10.2205/2020ES000730>, 2020.

865 Tian, J., Yang, Q., and Zhao, W.: Enhanced diapycnal mixing in the South China Sea, *Journal of*
866 *Physical Oceanography*, 39, 3191-3203, <https://doi.org/10.1175/2009jpo3899.1>, 2009.

867 Tu, J., Fan, D., Lian, Q., Liu, Z., Liu, W., Kaminski, A., and Smyth, W.: Acoustic observations of
868 Kelvin - Helmholtz billows on an Estuarine Lutocline, *Journal of Geophysical Research: Oceans*,
869 125, <https://doi.org/10.1029/2019jc015383>, 2019.

870 Vlasenko, V. and Hutter, K.: Numerical experiments on the breaking of solitary internal waves over a
871 slope–shelf topography, *Journal of Physical Oceanography*, 32, 1779-1793,
872 [https://doi.org/10.1175/1520-0485\(2002\)032<1779:NEOTBO>2.0.CO;2](https://doi.org/10.1175/1520-0485(2002)032<1779:NEOTBO>2.0.CO;2), 2002.

873 Voet, G., Alford, M. H., MacKinnon, J. A., and Nash, J. D.: Topographic form drag on tides and low-
874 frequency flow: observations of nonlinear lee waves over a Tall Submarine Ridge near Palau,
875 *Journal of Physical Oceanography*, 50, 1489-1507, <https://doi.org/10.1175/jpo-d-19-0257.1>, 2020.

876 Wang, Y.-H., Dai, C.-F., and Chen, Y.-Y.: Physical and ecological processes of internal waves on an
877 isolated reef ecosystem in the South China Sea, *Geophysical Research Letters*, 34,
878 <https://doi.org/10.1029/2007gl030658>, 2007.

879 Whalen, C. B., Talley, L. D., and MacKinnon, J. A.: Spatial and temporal variability of global ocean
880 mixing inferred from Argo profiles, *Geophysical Research Letters*, 39,
881 <https://doi.org/10.1029/2012gl053196>, 2012.

882 Wijesekera, H. W., Wesson, J. C., Wang, D. W., Teague, W. J., and Hallock, Z. R.: Observations of flow
883 separation and mixing around the Northern Palau Island/Ridge, *Journal of Physical Oceanography*,
884 50, 2529-2559, <https://doi.org/10.1175/jpo-d-19-0291.1>, 2020.

885 Xu, Z., Yin, B., Hou, Y., Fan, Z., and Liu, A. K.: A study of internal solitary waves observed on the
886 continental shelf in the northwestern South China Sea, *Acta Oceanologica Sinica*, 29, 18-25,
887 <https://doi.org/10.1007/s13131-010-0033-z>, 2010.

888 Xu, Z., Liu, K., Yin, B., Zhao, Z., Wang, Y., and Li, Q.: Long-range propagation and associated
889 variability of internal tides in the South China Sea, *Journal of Geophysical Research: Oceans*, 121,
890 8268-8286, <https://doi.org/10.1002/2016JC012105>, 2016.

891 Xu, Z., Wang, Y., Liu, Z., McWilliams, J. C., and Gan, J.: Insight into the dynamics of the radiating
892 internal tide associated with the Kuroshio Current, *Journal of Geophysical Research: Oceans*, 126,
893 e2020JC017018, <https://doi.org/10.1029/2020JC017018>, 2021.

894 Yang, Q., Tian, J., Zhao, W., Liang, X., and Zhou, L.: Observations of turbulence on the shelf and slope
895 of northern South China Sea, *Deep Sea Research Part I: Oceanographic Research Papers*, 87, 43-52,
896 <https://doi.org/10.1016/j.dsr.2014.02.006>, 2014.

897 Zhang, S. and Alford, M. H.: Instabilities in nonlinear internal waves on the Washington continental
898 shelf, *Journal of Geophysical Research: Oceans*, 120, 5272-5283,
899 <https://doi.org/10.1002/2014jc010638>, 2015.

900 Zhao, Z.: Satellite observation of internal solitary waves converting polarity, *Geophysical Research*
901 *Letters*, 30, <https://doi.org/10.1029/2003gl018286>, 2003.